Title
Approaching the Quantum Limit of Photodetection in Solid-State Detectors with Internal Signal Amplification

Author
Hall, David

Publication Date
2017

UNIVERSITY OF CALIFORNIA, SAN DIEGO

Approaching the Quantum Limit of Photodetection in Solid-State Detectors with Internal Signal Amplification

A dissertation submitted in partial satisfaction of the
requirements for the degree
Doctor of Philosophy

in

Electrical Engineering (Nanoscale Devices and Systems)

by

David Hall

Committee in charge:

Professor Yu-Hwa Lo, Chair
Professor Peter Asbeck
Professor Prabhakar Bandaru
Professor Zhaowei Liu
Professor Lu J. Sham

2017

The Dissertation of David Hall is approved, and it is acceptable in quality and form for publication on microfilm and electronically:

Chair

University of California, San Diego

2017

DEDICATION

To Wei

TABLE OF CONTENTS

LIST OF FIGURES

LIST OF TABLES

ACKNOWLEDGEMENTS

First, I would like to thank my advisor, **Professor Yu-Hwa Lo**, for the constant thoughtful guidance and encouragement throughout my PhD program. His breadth of experience, commitment to research, and dedication to student development is amazing and inspiring. I would also like to thank **Professor S.S. Lau** for warmly welcoming me to UCSD with open arms and mentoring me as I arrived here without connections or clear direction. I also thank my committee members. **Professor Peter Asbeck** has taught four of my classes and was an invaluable source of expertise for both courses and research. **Professors Prabhakar Bandaru and Zhaowei Liu** have also taught me during my first year and provided insightful feedback on research. **Professor Lu Sham** has also worked with me through many group meetings on the physical and theoretical aspects of my research.

I also need to thank my **former labmates**, who lighted the way for me. Dr. James Cheng spent time with me in the lab during my first year and challenged me to think critically. I worked closely with Dr. Samia Nawar Rahman during my first years here; she was always willing to help and encourage me, even after she graduated. Zhe Mei, Dr. Yuchun Zhou and Yi-Che Chen also helped me and were great labmates. I also had the pleasure of interacting with Dr. Arthur Zhang, Dr. Ash Arianpour, Dr. Sung Hwan Cho, Dr. Wen Qiao, Ti-Hsuan Ku, Jie Dai, Dr. T.F. Wu, and Dr. Sifang You, who provided valuable advice. Finally, Dr. Baoxia Li was not only a collaborator but also a truly wonderful mentor during her one year stay here.

Next, I need to thank **The Mighties**: Dr. Yu-Hsin Liu, who always helps me, always has a positive attitude, and is a great leader, Alex Zhang, Iftikhar Ahmad Niaz, Lujiang Yan, Mahmut Sami Kavrik, Yugang Yu, Mohammad Abu Raihan Mia, Zihan Xu, Li-Yuan Chiang, and Jiayun Zhou. I could not have asked for better colleagues and friends during my PhD. There are also **additional Mighties** in our research group I would like to thank for their help, friendship and support: Roger Chiu, Tony Yen, Tiantian Zhang, Ping-Wei Chen, Yuanyuan Han, Yi-Huan Tsai, Ramkumar Subramanian, Xin Fu, Yi Gu, Samir Damle, and Brian Lewis.

I would like to thank my **old friends**, who were there with me in spirit during my PhD. Talking to them and seeing them during breaks was very valuable to me.

Finally, I need to thank my **family**. My parents, Professor Lawrence Hall and Dr. Paula Petti were with me every step of the way. My brother, Geoffrey Hall is also very supportive. My uncle, Dr. Chris Petti, and aunt, Dr. Lisa Petti, were also a great source of both technical knowledge and moral support. My grandmother, Claire Petti, and late grandfather, Leo Petti, also never failed to support me. Last but not least, I thank my **wife**, Wei Cai, for her love and patience.

Portions of Chapter 2 have been published in the following publications: S. N. Rahman, D. Hall, Z. Mei, and Y. H. Lo, "Integrated 1550 nm photoreceiver with built-in amplification and feedback mechanisms," Optics Letters 38, 20 (2015); S. N. Rahman, D. Hall, Z. Mei, and Y. H. Lo, "Multiple gain mechanisms integrated in APDs biased below breakdown for sensitivity improvement," Proceedings of the

SPIE 8727, 87270P-1 (2013); D. Hall, Y. H. Liu, and Y. H. Lo, “Single photon avalanche detectors: prospects of new quenching and gain mechanisms,” Nanophotonics 4, pp. 397-412 (2015). The dissertation author was the second author/primary investigator and author of these papers.

Portions of Chapter 4 have been published in the following publications: Y. H. Liu, L. Yan, A. C. Zhang, D. Hall, I. A. Niaz, Y. Zhou, L. J. Sham, and Y. H. Lo, “Cycling excitation process: An ultra efficient and quiet signal amplification mechanism in semiconductor,” Applied Physics Letters 107, 053505 (2015); D. Hall, B. Li, Y. H. Liu, L. Yan, and Y. H. Lo, “Complementary metal-oxide-semiconductor compatible 1060 nm photodetector with ultrahigh gain under low bias,” Optics Letters 40, 19 (2015). For these papers, the dissertation author was a coauthor/ primary investigator and author.

Portions of Chapter 5 are currently being prepared for submission for publication of the material. L. Yan, Y. Yu, A. C. Zhang, D. Hall, I. A. Niaz, M. A. R. Miah, Y. H. Liu, and Y. H. Lo, “An amorphous silicon photodiode with 2 THz gain-bandwidth product based on cycling excitation processes”; D. Hall, Y. H. Liu, L. Yan, Y. H. Lo, “Approaching the quantum limit of photodetection in solid state photodetectors,” IEEE Transactions on Electron Devices. The dissertation author was a coauthor/primary author of this material. The dissertation author would also like to acknowledge Professor Julio Barreiro and Paul Lauria for assistance in PCB layout and purchase.

VITA

2011	Bachelor of Science, University of California, Berkeley Engineering Physics
2013	Master of Science, University of California, San Diego Electrical Engineering (Nanoscale Devices and Systems)
2017	Doctor of Philosophy, University of California, San Diego Electrical Engineering (Nanoscale Devices and Systems)

PUBLICATIONS

1. **D.Hall**, Y.H. Liu, L. Yan, Y. Yu, Y.H. Lo, “Approaching the quantum limit of photodetection in solid state photodetectors,” IEEE Transactions on Electron. Devices, Submitted.

2. M. A. R. Miah, I. A. Niaz, Y.H. Liu, **D. Hall**, and Y.H. Lo, “A high-efficiency low-noise signal amplification mechanism for photodetectors,” Proceedings of the SPIE 10108 (2017).

3. **D. Hall**, B. Li, Y.H. Liu, L. Yan, Y.H. Lo, “Complementary metal-oxide-semiconductor compatible 1060 nm photodetector with ultrahigh gain under low bias,” Optics Letters 40, 19 4440-4443 (2015).

4. **D. Hall**, Y.H. Liu, Y.H. Lo, “Single photon avalanche detectors: prospects of new quenching and gain mechanisms,” Nanophotonics 4: 397-4312 (2015).

5. Y.H. Liu, L. Yan, A. Zhang, **D. Hall**, I. Niaz, Y.Zhou, L.J. Sham, Y.H. Lo, “Cycling excitation process: an ultra efficient and quiet signal amplification mechanism in semiconductor,” Applied Physics Letters 107, 053505 (2015).

6. Y. Zhou, Y.H. Liu, S.N. Rahman, **D. Hall**, L.J. Sham, Y.H. Lo, “Discovery of a photoresponse amplification mechanism in compensated PN juctions,” Applied Physics Letters 106, 031103 (2015).

7. S.N. Rahman, **D. Hall**, Y.H. Lo, “Non-Geiger mode single photon detector with multiple amplification and gain control mechanisms,” Journal of Applied Physics 115, 173104 (2014).

8. S.N. Rahman, **D. Hall**, Z. Mei, Y.-H. Lo, “Integrated 1550nm photoreceiver with built-in amplification and feedback mechanisms,” Optics Letters 38, 20 (2013).

9. S.N. Rahman, **D. Hall**, Z. Mei, Y.-H. Lo, “Negative feedback and multiple gain mechanisms for sensitivity improvement in 1550nm optical detection,” IEEE Photonics Conference, 978-1-4577- 1507-5 (2013).

10. S. N. Rahman, **D. Hall**, Z. Mei, Y.-H. Lo, “Multiple gain mechanisms integrated in APDs biased below breakdown for sensitivity improvement,” Proceedings of the SPIE 8727, 87270P (2013).

ABSTRACT OF THE DISSERTATION

Approaching the Quantum Limit of Photodetection in Solid-State Detectors with Internal Signal Amplification

by

David Hall

Doctor of Philosophy in Electrical Engineering (Nanoscale Devices and Systems)

University of California, San Diego, 2017

Professor Yu-Hwa Lo, Chair

This thesis offers three physical device concepts to overcome limitations in conventional solid-state photodetectors. Tradeoff between sensitivity, bandwidth and dynamic range is a pressing issue for detectors that must meet the demands of imaging and communications applications. Single photon sensitivity has long been possible in a solid-state detector, but with no dynamic range at the device level, and bandwidth on the order of 10 MHz, far below the requirements for modern communications. Detectors reaching 40 GHz bandwidth and exceeding 20 dB dynamic range are now in wide use, but the fundamental physics of these devices limits the sensitivity to only 1000 photons in practical operating conditions. This thesis presents theoretical and experimental progress in three main thrusts that are promising in developing a detector that can maintain large dynamic range and high bandwidth while reaching the ultimate sensitivity limit of a single photon.

The first device covered is a device which incorporates multiple gain mechanisms in a single device. Rather than relying solely on avalanche gain, this device incorporates bipolar gain which relaxes the excess noise burden experienced by conventional avalanche detectors. Negative feedback is also shown to play a role in regulating the gain and reducing noise.

The second and third device concepts utilize localized states in disordered material to exploit a host of physical phenomena. Localized states are known to increase carrier excitation probability by relaxing the k-selection rule of momentum conservation. Auger excitation and electron phonon coupling play a role in this new internal signal amplification mechanism, called Cycling Excitation Processes (CEP).

CEP is first presented in crystalline silicon, where localization is achieved through heavy doping and partial compensation. Impressive performance in terms of gain, responsivity and noise are promising for realizing the goal of a next generation solid-state detector approaching the quantum limit.

Despite the merits, CEP in crystalline silicon suffers from high dark current due to heavy doping. Amorphous silicon is presented as an alternative means of achieving localization to realize CEP. High speed and high sensitivity capability is demonstrated. While the work is ongoing as of the writing of this thesis, a clear research plan is in place for realizing an amorphous silicon CEP detector capable of high bandwidth and single photon detection.

Chapter 1 Introduction

1.1 Principles of Photodetection

Detection of light is a requirement for many areas of everyday life, as we can obtain critical information about our environment by converting light into a measurable signal. The advent of optical fibers has allowed communication to occur via pulses of light, which are converted into an electrical signal, recorded as a binary 1 or 0. Biomedical applications also require photodetectors in the visible wavelength region for high contrast and sensitive imaging [1]. Telecommunications require infrared photodetectors for far range communication [2]. Near-IR wavelength detectors such as 1060nm photodetectors also find use in security, defense, and medical laser treatment.

The smallest divisible unit of light is a photon, which is a quantum of electromagnetic radiation. While optical fiber communications typically use packets on the order of or exceeding 1000 photons to represent a bit of information [3], some situations call for photodetectors that are sensitive to a single photon. Single photon detectors are used in deep space communication where the signal to be detected is extremely weak. The emerging field of quantum communication also requires ability to detect a single photon [4].

1.2 Solid-State Photodetectors

Solid state photodetectors made from semiconducting material are the primary detectors used today due to their scalability and potential integration with other mature processes. Photodetectors at the 850nm, 1310nm and 1550nm wavelength bands are the receiving component in optical fiber communications systems. Solid state detectors for fiber optic communications commonly use InGaAs and InP for light absorption and carrier transport, respectively [5]. Photodetectors incorporating silicon have also been explored extensively due to potential for integration of photonics with existing CMOS processes.

1.2.1 Photodetector Requirements

For a photodetector to yield a detectable signal, it should have a high responsivity, which is the amount of output current it is capable of producing for a given optical input. It is expressed as

$$R = \frac{Output\ current}{Input\ power} = QE \cdot \frac{q\lambda}{hc} \qquad (1.1)$$

where h is Planck's constant, q is the electron charge, λ is the photon wavelength, and the corresponding photon energy is hc/λ. The QE is the quantum efficiency of the device, which represents the percentage of incident photons that generate an electron-hole pair. QE is also defined as the ratio of the electron generation rate to photon incidence rate, from which the above expression can also be derived. Quantum efficiency can further be separated into external quantum efficiency (EQE) in which the incident photons are considered to be those photons that are impinging on the device active area, and internal quantum efficiency (IQE) in which the incident photons are considered to be only those photons that are absorbed by the material.

For a photodetector to have high resolution, it should have linearity in its output response. This means the photocurrent, the difference between the current under illumination and the current under dark condition, should vary roughly linearly with the input number of photons.

For a photodetector to result in a high signal to noise ratio, it should produce low noise. In the ideal case, the noise of a photodetection system would be limited by the thermal noise of the electronic readout circuit and not by the noise in the detector itself.

1.2.2 Photodiode Principles

A photodiode is a semiconductor material with a p-n junction created by electrical doping. Photons absorbed in the semiconductor generate electron-hole pairs via the photoelectric effect, by which light of a minimum frequency incident on a certain material can cause electron ejection from the material. Semiconductors are characterized by quasi-continua of states, or bands, arising from the periodicity of the lattice. Two such bands in semiconductors are called the conduction band, mostly filled states at lower energy, and the valence band, mostly vacant states at higher energy, separated by a forbidden gap called the band gap, in which there are no delocalized states that can lead to current. Light with energy exceeding the band gap energy can excite electrons from the valence band to the conduction band where they occupy delocalized states. These free carriers are then separated by the built in electric field across the p-n junction and collected at electrodes as current. The photocurrent is determined by the generation rate and absorption rate . Photodiodes provide limited sensitivity since the responsivity is limited.

1.2.3 Avalanche Photodiode: Sub-Geiger Mode

A common solid state photodetector is the Avalanche Photodiode (APD). APDs are biased close to their reverse bias breakdown voltage where impact ionization provides gain in the form of carrier multiplication. Photons are absorbed in an absorption region, a layer made of a material with a suitable bandgap for the wavelength of light to be detected, and generate electron-hole pairs. These pairs are swept by an electric field into a multiplication region where the carriers undergo acceleration in order to have sufficient probability of initiating impact ionization. Secondary charge carriers generated by impact ionization can themselves be accelerated and initiate further ionization events. Impact ionization rates for electrons and holes are given by equations (1.2a) and (1.2b), respectively, and represent the number of electron-hole pairs generated per unit distance by a single carrier traveling through the multiplication region.

$$\alpha = \alpha_0 e^{-[\frac{c_n}{E}]^{m_n}} \tag{1.2a}$$

$$\beta = \beta_0 e^{-[\frac{c_p}{E}]^{m_p}} \tag{1.2b}$$

α_0, β_0, c_n, c_p, m_n, m_p are all ionization coefficients which can be determined empirically for a given material to give the ionization rate as a function of electric field, for example for Indium Phosphide [6], and silicon [7]. These impact ionization events lead to an internal gain which results in a detectable electrical signal with the use of a preamplifier. The impact ionization process is shown in Fig. 1.1, where the ionization coefficients label schematically the average distance for electrons and holes to initiate impact ionization.

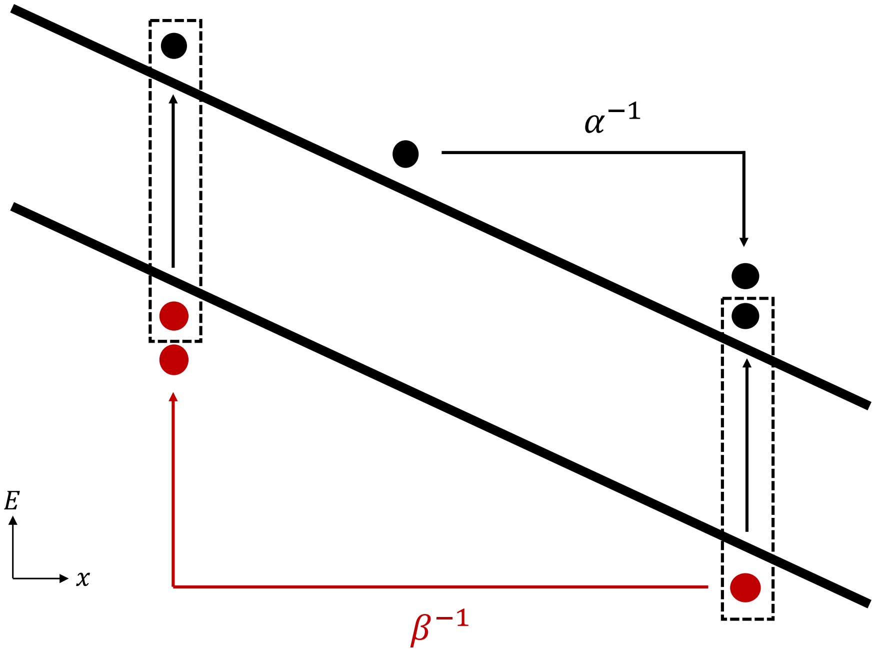

Figure 1.1: Energy versus distance schematic of the impact ionization process for electrons (black) and holes (red).

The multiplication region is ideally made of a material in which either electrons or holes have a significantly higher probability of generating an impact ionization event [8]. In this case, the carrier multiplication process is much more predictable than if electrons and holes had similar probability of initiating impact ionization. In the former case, the noise associated with impact ionization, excess noise, is much smaller. This concept is quantified by the k ratio, the ratio between electron and hole ionization rates, or hole and electron ionization rates, whichever ratio yields a value less than 1.

$$k_{eff} = \begin{cases} \frac{\alpha}{\beta}, \ \alpha < \beta \\ \frac{\beta}{\alpha}, \ \alpha > \beta \end{cases} \tag{1.3}$$

It is desirable to design an APD with a multiplication region whose k ratio is as small as possible to minimize the excess noise. The period of time during which impact ionization occurs in the APD represents an optically dead time during which no further photons can be resolved, since there would be no way to distinguish between the photogenerated carriers due to the newly arrived photons and the impact ionization events resulting from the previously arrived photons. No further photons can be detected until the impact ionization events are quenched. Quenching can occur naturally, as the number of carriers left in the multiplication region becomes very small compared to the probability of a given carrier initiating an ionization event. Quenching can also occur with the aid of an external quenching circuit which forces a certain electric field across the multiplication region to reduce ionization probability [9].

While the bias of an APD is close to breakdown voltage, the bias is kept below breakdown voltage, a mode of operation commonly called sub-geiger mode or linear mode. These names arise because the output signal is roughly linear over a wide range of input optical power, meaning APDs can be used for photon number resolving. InP based APDs are commonly employed in optical fiber communication systems, conventionally reaching speeds as high as 10GHz, beyond which the gain-bandwidth product degrades [10].

1.2.4 Single Photon Avalanche Detector: Geiger Mode

One solid-state photodetector capable of detecting single photons is the Single Photon Avalanche Diode (SPAD). SPADs, like APDs, rely on impact ionization for internal gain, but operate above their breakdown voltage, a mode of operation called geiger mode, in order to achieve very large internal gain, which allows them to be single photon sensitive. Geiger mode, however, like the name suggests, does not allow any photon number resolving capability; it only allows detection of one or more photons but not the ability to determine how many photons led to the detection event.

1.2.5 APD and SPAD Limitations

While APDs are biased below breakdown voltage in order to offer both dynamic range and high bandwidth suitable for fiber optic communications, the sensitivity is limited by the excess noise associated with impact ionization, to be discussed in the next section. This excess noise limits the practical gain that can be achieved in most operating conditions. On the other hand, while SPADs offer single photon sensitivity, they only meant to be operated above the breakdown voltage, which leaves no room for dynamic range [11]. There would be great use for a photodetector that has both single photon sensitivity and high linearity. Furthermore, if such a detector could operate at low bias well below what APDs or SPADs are capable of, CMOS integration could become a possibility.

1.3 Photodetector Noise

The limiting factor of any gain mechanism is typically the noise associated with that mechanism. Thus, it is useful to first review the sources of noise in photodiodes and then introduce the excess noise factor of APDs arising from multiplication gain.

1.3.1 Sources of Noise in a Photodetector

Thermal noise arises due to random motion of electrons in a conductor. External loads including preamplifiers contribute thermal noise to the receiver system. The thermal noise is given by

$$\sigma_T = \frac{4k_BT}{R_L}F_N \left[\frac{A^2}{Hz}\right] \tag{1.4}$$

where F_N is the amplifier noise figure and R_L is the load resistance.

Shot noise arises from the random photogeneration of electron-hole pairs in the photodetector. The fluctuation in the current due to this random generation should realistically be described by Poisson statistics. However, if the incident photon number is large enough the fluctuation can be approximated by a Gaussian distribution [1]. The shot noise power density for a photodiode is then given by

$$\sigma_S = 2e\left(I_d + I_{ph}\right)\left[\frac{A^2}{Hz}\right] \tag{1.5}$$

where Id is the dark current, or current in the absence of illumination, and Iph is the photocurrent, or the current that is due to light absorption. The photocurrent is the remaining current after subtracting the dark current. Thus, Id + Iph gives the total current flowing in the photodiode.

1.3.2 Excess Noise

The ability to achieve high gain in an APD comes at a cost in the form of excess noise, which is the noise associated with impact ionization. In an APD, the primary current, which is the device current under the condition of unity gain, is amplified by a factor of M, the multiplication gain. Thus, the current of an APD biased to gain M will have a total current of $M(I_{d_0} + I_{ph_0})$, where $(I_{d_0} + I_{ph_0})$ is the current the device would have at unity gain, M=1. Id0 and Iph0 are the primary dark current and primary photocurrents, respectively, and are the dark current and photocurrent at the unity gain condition. However, the shot noise is amplified by the same factor M. Thus, an ideal APD with no excess noise would have a shot noise of

$\sigma_S = 2eM^2(I_{d_0} + I_{ph_0})\ [\frac{A^2}{Hz}]$. The excess noise factor is the factor by which the signal noise increases compared to that in which there is no multiplication noise [McIntyre advances]. By using rate equations and treating electron and hole current fluctuations described above as random variables, McIntyre showed [12] that the shot noise and excess noise factor are given by

$$\sigma_S = 2eM^2F(M)\left(I_{d_0} + I_{ph_0}\right)\left[\frac{A^2}{Hz}\right] \qquad (1.6a)$$

$$F(M) = k_{eff}M + (1 - k_{eff})(2 - \frac{1}{M}) \qquad (1.6b)$$

where F(M) is the excess noise factor, which is a function of multiplication gain.

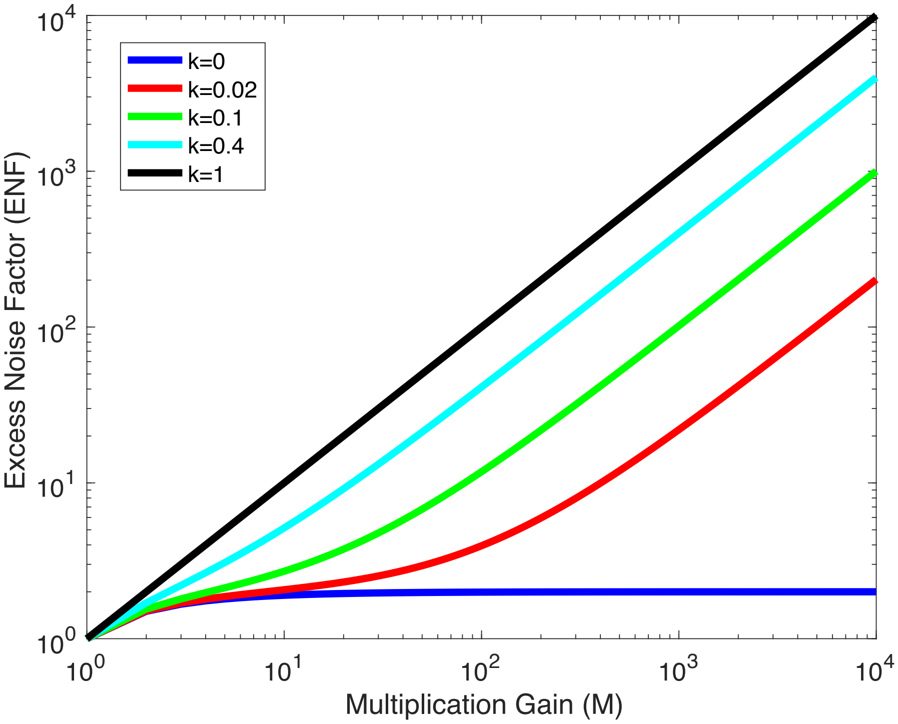

Figure 1.2: Excess noise factor (ENF) as a function of multiplication gain (M) for various k values.

Fig. 1.2 shows the excess noise factor as a function of multiplication gain for different keff. Keff for silicon is 0.02. The theoretical limit of the APD excess noise factor under the condition of gain approaching infinity is 2. This figure demonstrates a fundamental limitation in APDs, which is that the practical gain that can be achieved in an APD is limited by excess noise, which becomes severe at higher gain. Because of this, APDs are typically operated at a relatively low gain in the thermal noise limit. Thermal noise, unlike shot noise, is not enhanced by a factor of M, thus, the signal to noise ratio is enhanced by a factor of M^2 when operated in the thermal noise limit [1]. On the other hand, if the detector is operated at higher gain in the shot noise limit, the SNR is degraded by a factor of the excess noise factor F(M).

1.4 Dissertation Outline

Solid state photodetectors used today have fundamental limitations. The responsivity of photodiodes is limited due to unity gain operation. SPADs are not capable of photon number resolving and often require high power operation and complicated external circuits to prevent thermal runaway. APDs can achieve only limited gain and hence sensitivity due to the excess noise penalty at high gain.

This dissertation aims to address these limitations by fundamentally changing how gain is achieved internally in the device. The next chapter will survey the achievement in combining multiple gain mechanisms in a single device, which pushes APD sensitivity close to the quantum limit of photodetection. The subsequent chapters explore a new gain mechanism not previously used in photodetectors. Gain is achieved by introducing disorder in the material. This creates localized states that relax the momentum conservation requirement and allow a process similar to but distinct from impact ionization to occur. The dissertation then finishes by exploring the areas which could be significantly impacted by a new class of photodetector on the brink of the quantum limit of photodetection, and the future direction for this research.

References:

1. R. Cubeddu, D. Comelli, C. D'Andrea, P. Taroni, and G. Valentini, "Time-resolved fluorescence imaging in biology and medicine," Journal of Physics D: Applied Physics **35** pp. 61-76 (2002)

2. H. Hemmati, A. Biswas, and I. B. Djordjevic, "Deep-space optical communications: future perspectives and applications," Proceedings of the IEEE, **99**(11) pp. 2020-2039 (2011).

3. G. P. Agrawal, *Fiber-Optic Communication Systems*. N.Y.: John Wiley & Sons, Inc., 1992.

4. R. H. Hadfield, "Single-photon detectors for optical quantum information applications," Nature Photonics **3**, 12, pp. 696-705 (2009).

5. J. C. Campbell, "Recent advances in telecommunications avalanche photodiodes" Journal of Lightwave Technology **25**, 1 (2007).

6. M. A. Saleh, M. M. Hayat, P. P. Sotirelis, A. L. Holmes, J. C. Campbell, B. E. A. Saleh, and M. C. Teich, "Impact-ionization and noise characteristics of thin III-V avalanche photodiodes," IEEE Transactions on Electron Devices **48**, 12 (2001).

7. R. Van Overstraeten and H. De Man, "Measurement of the ionization rates in diffused silicon p-n junctions," Solid-State Electronics **13**, p.p. 583-608(1970).

8. J. C. Campbell, S. Demiguel, F. Ma, A. Beck, X. Guo, S. Wang, X. Zheng, X. Li, J. D. Beck, M. A. Kinch, A. Huntington, L. A. Coldren, J. Decobert, and N. Tscherptner, "Recent advances in avalanche photodiodes," IEEE Journal of Selected Topics in Quantum Electronics **10,** 4 (2004).

9. S. Cova, M. Ghioni, A. Lotito, I. Rech, and F. Zappa, "Evolution and prospects for single-photon avalanche diodes and quenching circuits," Journal of Modern Optics, **51**, 9-10, pp. 1267-1288 (2004).

10. Y. Kang, H. D. Liu, M. Morse, M. J. Paniccia, M. Zadka, S. Litski, G. Sarid, A. Pauchard, Y. H. Kuo, H. W. Chen, W. S. Zaoui, J. E. Bowers, A. Beling, D. C. McIntosh, X. Zheng, and J. C. Campbell, "Monolithic germanium/silicon avalanche photodiodes with 340 GHz gain-bandwidth product," Nature Photonics **3**, p.p. 59-63 (2009).

11. M. A. Itzler, R. Ben-Michael, C. F. Hsu, K. Slomkowski, A. Tosi, S. Cova, F. Zappa, and R. Ispasoiu, “Single photon avalanche diodes (SPADs) for 1.5 um photon counting applications,” Journal of Modern Optics **54**, 2-3, pp. 283-304 (2007).

12. R. J. McIntyre, “Multiplication noise in uniform avalanche diodes,” IEEE Transactions on Electron Devices **ED-13**, 1 (1966).

Chapter 2 Enhanced Sensitivity using Multiple Gain Mechanisms

As discussed previously, a solid state detector that relies exclusively on impact ionization for internal gain will have limited gain and sensitivity due to the excess noise associated with multiplication gain. Noise reduction could be achieved by using additional gain mechanisms that do not incur impact ionization noise. Using multiple gain mechanisms can reduce the noise for two key reasons. First, with an additional gain mechanism, the contribution of impact ionization required to achieve a certain gain is reduced. With more than one gain mechanism contributing to the total gain, the same total gain can be achieved with lower impact ionization excess noise compared to a device that only uses impact ionization for internal gain. Second, the different gain mechanisms that contribute to the total gain are not independent of each other, but rather influence each other through negative feedback such that no single gain mechanism dominates. The term created to describe these effects is Multiple Amplification Gain with Internal Control (MAGIC) and has been implemented in a working device. The ultimate goal of the MAGIC detector is to create a large dynamic range single photon sensitive device operating in free running mode with no external quenching.

2.1 MAGIC Detector Concepts

2.1.1 Multiple Gain Mechanisms

The MAGIC detector design facilitates impact ionization through a p-n diode for the first stage of gain, as in a traditional APD. The second stage of gain is provided by a different current amplification mechanism. One such candidate is bipolar gain, in which a heavily doped emitter emits electrons across a (traditionally) lightly doped base and into a collector. Devices called bipolar transistors employ an emitter-base-collector structure as either n-p-n doped or p-n-p doped, respectively. In an n-p-n structure, a small base current is amplified by a factor of beta into a much larger collector current, in the form of electron injection from the emitter into the base where they are then collected in the collector. The gain factor beta is defined as the ratio of collector current to base current.

While the base doping is traditionally very light, the MAGIC detector uses moderate base doping for two reasons. First, as the n-p-n bipolar structure and the p-n avalanche diode are monolithically incorporated into the same device, the p-n component must be shared between the bipolar and avalanche diode structure. That is, the avalanche diode can be considered to be in parallel with the bipolar base-collector. It is not feasible to use extremely light doping in the p-region of the diode since large electric fields are required to initiate impact ionization. Second, although beta is typically between 100 to 200 in bipolar transistors, such a high bipolar gain is not necessary in the MAGIC detector since the purpose of the bipolar gain is to reduce the necessary contribution of impact ionization multiplication gain and not to provide the majority component of the gain. In fact, if the bipolar gain is too large with respect to the multiplication gain, the device can enter an unstable mode of operation exhibited by self-pulsation after the initial photon pulse.

2.1.2 Internal Control

Whereas SPADs require either gated mode operation or free-running with external quenching circuits, the MAGIC concept promises a detector operating in linear, free-running mode with no external quenching circuit that can approach the sensitivity limit of single photon. This requires that the MAGIC detector must not only be capable of producing high gain but also internally controlling the gain. This can be accomplished through bandgap engineering using heterojunction interfaces between different semiconducting materials. A generalized example of bandgap engineering for any semiconductor material system is explained below for a coupled multiplication-bipolar (n-p-n) MAGIC detector, and shown in Fig. 2.1.

The first stage of gain in a MAGIC detector will be impact ionization in a p-n diode. Both the magnitude of the gain and the extent to which the device can quench the avalanche pulse and reset to a photon sensitive mode depends on the electric field across the p-n multiplication region. This electric field can be controlled through a heterojunction valence band (VB) offset at the p-type side of the multiplication region. This VB offset will trap holes and create a sheet charge at the heterojunction interface. The larger this sheet charge density, the smaller the electric field across the multiplication region and the smaller the probability of energetic carriers traversing the multiplication region to initiate impact ionization. Thus, increasing the VB energy offset between the two materials on either side of the junction will lead to faster quenching. The reset time of the device is then determined by the hole escape time from the VB offset, affected by both thermal excitation over the barrier and quantum mechanical tunneling through the barrier.

The second stage of gain in a multiplication-bipolar MAGIC detector is bipolar gain, provided by a heavily doped emitter. In order to control the degree of bipolar injection, a conduction band offset is used between the emitter and the multiplication region. The conduction band (CB) offset acts as an energy barrier that the injected electrons must overcome.

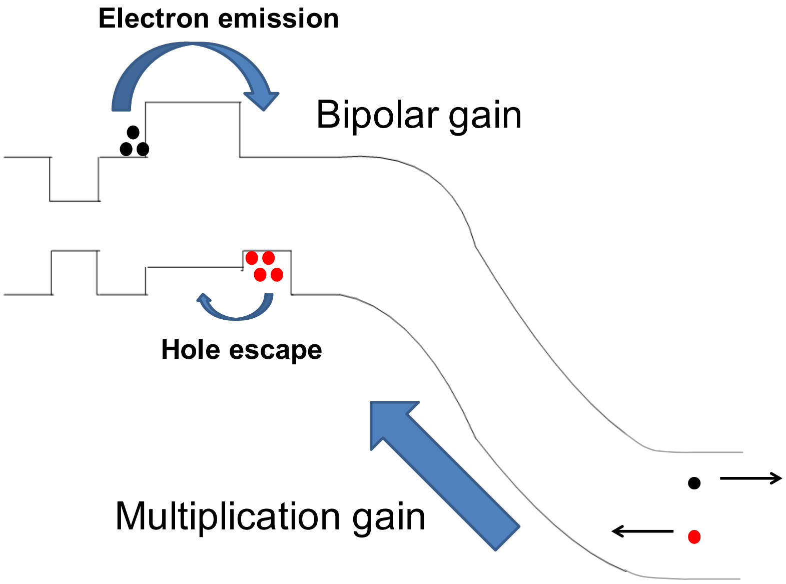

Figure 2.1: MAGIC detector band diagram showing electron (black) and hole (red) dynamics.

While the VB offset can be conceptually understood as controlling the avalanche gain and the CB offset as controlling the bipolar gain, the real situation is far more complex due to the interaction between the two gain mechanisms and the way they influence each other. First, the sheet charge density at the VB offset not only controls the impact ionization probability but also controls the electron injection from the emitter. Second, electrons injected from the emitter into the multiplication region can initiate impact ionization and contribute to multiplication gain. These effects counterbalance each other. For example, a large sheet charge density will reduce the instantaneous multiplication gain as a result of a lower electric field across the multiplication region. However, a large sheet charge density will also attract a larger electron injection, and those injected electrons can initiate impact ionization which causes a larger instantaneous multiplication gain. Likewise, a large electron injection will lead to a larger instantaneous multiplication gain, which in turn leads to a larger VB sheet charge density which tends to reduce the instantaneous multiplication gain.

In this manner, the avalanche gain, and hence the total gain, is controlled by negative feedback. Negative feedback is not only vital for self-quenching, but also for reducing the device noise. Noise due to multiplication gain arises due to the fact that multiplication gain is a random variable which fluctuates about its mean value. If the instantaneous gain is significantly lower than its mean value, the impact ionization process is allowed to continue with relatively high probability. If the instantaneous gain is significantly higher than its mean value, the impact ionization process is more likely to be quenched. Thus, negative feedback in an avalanche detector can play an important role in limiting the gain fluctuation and reducing the excess noise [1,2]. Multiple amplification mechanisms allows for a smaller multiplication gain and hence smaller excess noise. Negative feedback allows for self-quenching and smaller noise through gain control. However, these two components of the MAGIC concept, multiple amplification mechanisms, and negative feedback, are not independent phenomena but closely related.

2.2 MAGIC Detector Design Optimization

Since the gain mechanisms involved in a MAGIC detector are coupled, it is important to optimize the relative strengths of the gain mechanisms through bandgap engineering in order to achieve desirable performance. While multiplication gain is the main mechanism involved in a MAGIC detector, if the multiplication gain is too large compared to the bipolar gain, the effects of negative feedback are reduced and there becomes little difference between the MAGIC detector and a conventional APD. If the bipolar gain is too large compared to the multiplication gain, the device behaves as a phototransistor.

The effects of multiplication gain and bipolar gain, and the way they interact with each other through negative feedback, can be modeled by introducing time constants for the electron and hole escape times, which was done in [3]. The electron escape time, τ_n, is related to electron injection from the emitter across the conduction band offset. The hole escape time, τ_p, is related to hole escape from the valence band offset at the end of the multiplication region, which occurs either through thermionic emission or tunneling.

Current continuity equations can be introduced for the MAGIC detector:

$$\frac{1}{v}\frac{\partial J_p(x,t)}{\partial t}+\frac{\partial J_p(x,t)}{\partial x}=\beta J_p+\alpha J_n \tag{2.1a}$$

$$\frac{1}{v}\frac{\partial J_n(x,t)}{\partial t}+\frac{\partial J_n(x,t)}{\partial x}=\beta J_p+\alpha J_n \tag{2.1b}$$

v is the saturation velocity of electrons and holes (assumed for simplicity to be equal), equal to 10^7 cm/s, J_n and J_p are the elecrtron and hole currents, and α and β are the electron and hole ionization coefficients defined in Chapter 1. The total current, which is independent of x, is expressed as

$$J=J_p(x)+J_n(x)+\frac{\varepsilon}{W}\frac{dV_M}{dt} \tag{2.2}$$

where V_M is the voltage drop across the multiplication region, and ε is the permittivity of the multiplication region, which for InP is taken as $12.4\varepsilon_0$.

Equations (2.1) and (2.2) can be solved by first enforcing boundary conditions specific to the MAGIC detector and next considering interfacial sheet charge densities at the electron and hole barriers. These barriers are shown in Fig X. W^- and W^+ refer to the sides of the hole barrier inside the multiplication region and outside the multiplication region, respectively. $W+L^-$ and $W+L^+$ refer to the sides of the electron barrier closer to the multiplication region and farther from the multiplication region, respectively. The unique hole currents are given by $J_p(W^-)$ and $J_p(W^+)$ while the unique electron currents are given by $J_n(W+L^-)$ and $J_n(W+L^+)$, respectively.

Thus, there are three unique boundary conditions that can be applied to the total current:

$$J = J_p(W^-) + J_n(W + L^-) + \frac{\varepsilon}{W}\frac{dV_M}{dt} \tag{2.3a}$$

$$J = J_p(W^+) + J_n(W + L^-) + \frac{\varepsilon}{L}\frac{d(V - V_M)}{dt} \tag{2.3b}$$

$$J = J_p(W^+) + J_n(W + L^+) \tag{2.3c}$$

Additionally, $J_p(W^+)$ and $J_p(W^-)$ can be expressed in terms ofτ_n, τ_p, the interfacial hole barrier sheet charge, P_i, and interfacial electron barrier sheet charge, N_i, respectively:

$$J_p(W^+) = \frac{eP_i}{\tau_p} \tag{2.4a}$$

$$J_n(W + L^-) = \frac{eN_i}{\tau_n} \tag{2.4b}$$

Charge continuity at the electron and hole barrier interfaces gives us:

$$\frac{\partial P_i}{\partial t} = \frac{1}{e}\left[J_p(W^-) - J_p(W^+)\right] \tag{2.5a}$$

$$\frac{\partial N_i}{\partial t} = \frac{1}{e}\left[J_n(W + L^+) - J_n(W + L^-)\right] \tag{2.5b}$$

The total current can be solved as

$$J = \frac{\varepsilon}{\tau_p}\left[\frac{1}{W} + \frac{1}{L}\right](V - V_M) + \frac{\varepsilon}{\tau_n L}(V - V_M) + \frac{\varepsilon}{L}\frac{d(V - V_M)}{dt} \tag{2.6}$$

By considering illumination with a photon flux given as $R = \frac{N_{ph}}{T}$ where N_{ph} is the photon number within a time period T, a steady state solution can be found for V_M:

$$V_M(\infty) = V - \frac{e\tau_p R}{\varepsilon}\frac{LW}{L+W}e^{AW}\left[\frac{\gamma\left(1-\frac{\beta}{\alpha}\right)}{e^{AW}-\left[1+\gamma\left(\frac{\beta}{\alpha}-1\right)\right]}\right] \tag{2.7}$$

The total steady state gain is then

$$G = \frac{J}{eR} = e^{AW}\left[\frac{(\gamma+1)\left(1-\frac{\beta}{\alpha}\right)}{e^{AW}-\left[1+\gamma\left(\frac{\beta}{\alpha}-1\right)\right]}\right] \tag{2.8}$$

A plot of the gain versus photon number is shown in Fig. 2.2 for both the model and experiment.

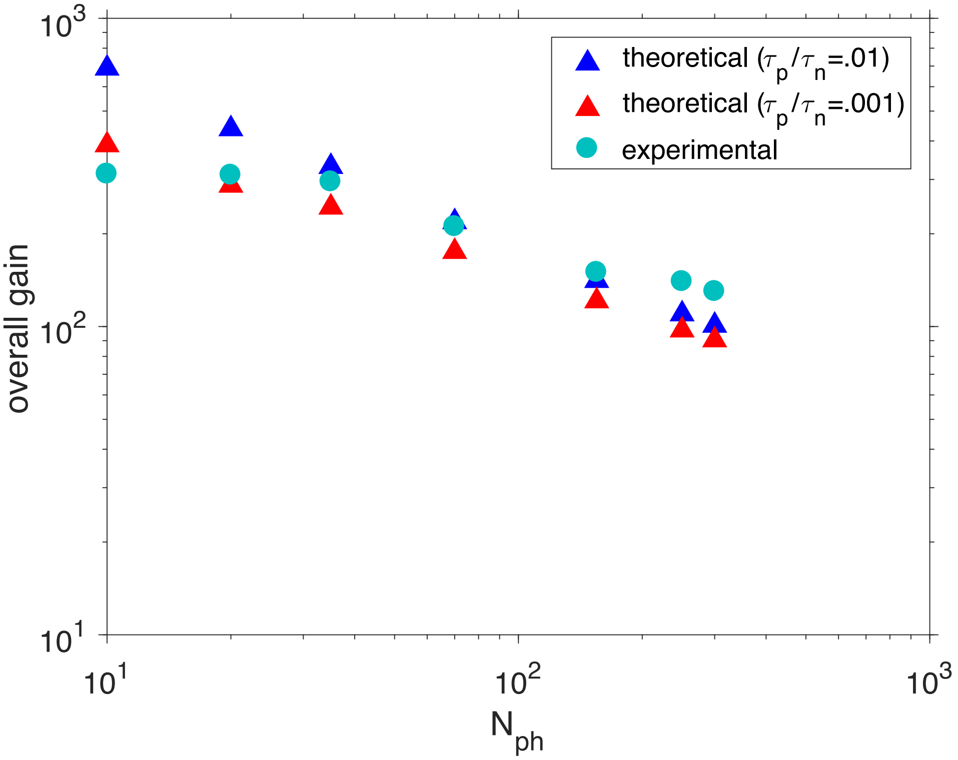

Figure 2.2: Gain versus photon number for theory and experiment for τ_p/τ_n values.

The stability of the device can be characterized by introducing parameters for the hole escape time and bipolar gain. For a given bipolar gain, γ, there is a bias voltage that determines the stable region of operation for the MAGIC detector. For a given operation bias, the effect of the bipolar gain can be seen on the total gain. If the bipolar gain is too small, the total gain of the device is uniform and corresponds to the gain of an APD.

2.3 MAGIC Detector Design Implementation

A MAGIC detector was implemented in the III-V material system and strongly validated the principles of the MAGIC design [4]. The detector, shown in Fig. 2.3, consists of an InGaAs absorption region, sensitive to 1550nm light, and InP multiplication region where the impact ionization occurs. The device thus employs a separate absorption multiplication (SAM) structure in which the light absorption and signal amplification occur in different materials. An applied bias creates an electric field across part or all of the multiplication region which leads to a high impact ionization probability. When the applied reverse bias voltage is large enough, the electric field extends all the way through the multiplication region and penetrates into the absorption region, separating the photogenerated carriers. The bias at which this happens is called the punch-through voltage and corresponds to unity multiplication gain, M=1. The multiplication gain increases from unity as the bias voltage is increased beyond the punch-through voltage. This design is commonly referred to as “reach through”.

The valence band offset at the p-type side of the multiplication region is created by a heterojunction between InGaAlAs and InAlAs, and is 100meV in magnitude [5]. The conduction band offset between the emitter and multiplication region is created by both a heterojunction between InP and InAlAs which is 286meV in magnitude[6] and a heterojunction between InP and InGaAs which is 270meV in magnitude [6].

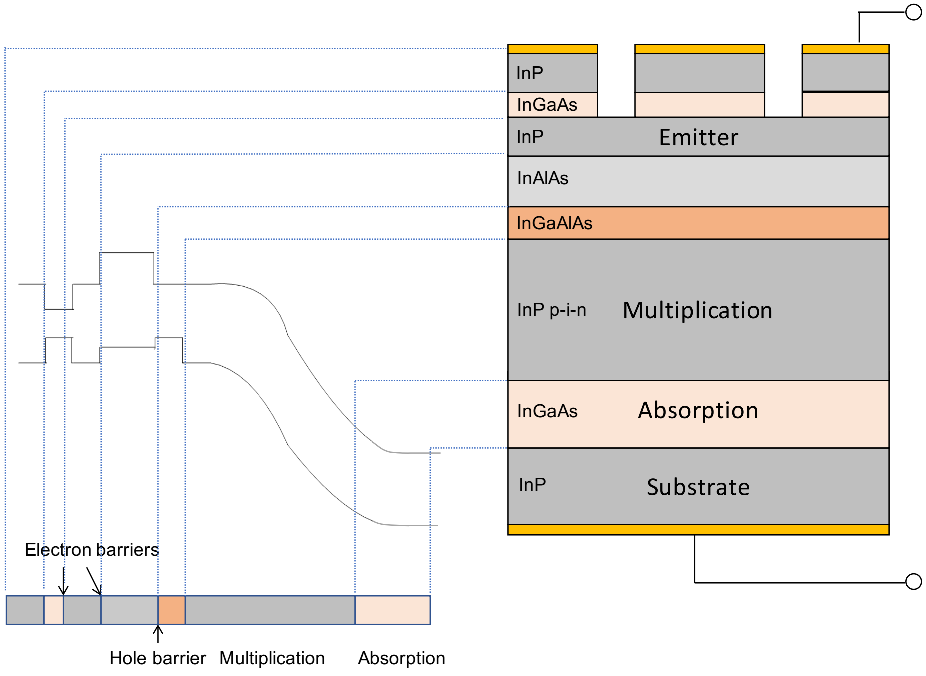

Figure 2.3: MAGIC detector cross section with epitaxial layers (right) and band diagram (left).

2.4 MAGIC Detector Experimental Results

2.4.1 MAGIC Detector Experimental Setup

The experimental setup used to characterize the MAGIC detector is described.

An Agilent 81110A pattern generator was used to trigger an iD Quantique id300 pulsed 1550nm wavelength laser. The laser is triggered at 250mV amplitude. The pulsewidth of the laser is 300ps. Neutral density filters are used for optical attenuation in order to achieve the desired optical power based on Poisson statistics of photon arrival. The device under test (DUT) was packaged and placed in a Janis VPF-100 cryogenic chamber for cooling. The device electrical output was connected to a bias tee. DC bias was applied to the device through the inductive port of the bias tee, while the AC response of the device was passed through the capacitive port. The capacitive port of the bias tee was passed to a cascaded LNA chain to amplify the signal to a detectable level. An attenuator was used to reduce electrical ringing. The subsequent output was then passed to an oscilloscope to detect impulse response.

2.4.2 MAGIC Detector Data Analysis

Data is obtained from the oscilloscope as a pulse train with multiple peaks. A counting histogram can be made versus the peak signal voltage, and this distribution can be fitted with a Gaussian distribution. By measuring this distribution for various photon numbers, the device dynamic range can be determined, as can the maximum sensitivity. Furthermore, the bit error rate for detecting a certain number of photons per pulse can be determined by comparing the overlap between that photon number distribution and the dark distribution.

For low photon numbers where it is difficult to resolve the voltage peak from the noise floor, digital signal processing can be used to enhance the sensitivity. The raw data was post processed using an infinite response comb filter of bandwidth 100kHz, Q factor of 10, repetition frequency of 1MHz, and sampling frequency of 2.5GHz. The filter output does not preserve the absolute magnitude of the signal response but substantially improves the sensitivity.

One effect of the filter is to artificially introduce spread in the peak response distribution, which would result in an overestimation of the bit error rate (BER). This noise was reduced by dividing the pulse train into groups of 10 pulses. The mean signal response within each group is calculated. Each signal peak in the pulse train is then normalized by multiplying by the ratio of the total pulse train mean (one mean for every peak) to the group mean (corresponding to that particular signal peak).

2.4.3 MAGIC Detector Performance

The counting histogram for peak signal response in arbitrary units is shown in Fig. 2.4. Different distributions are shown for different numbers of photons per pulse. The dark condition is represented by the 0 photon per pulse distribution. Each histogram is fitted with a Gaussian curve, from which the BER can be calculated.

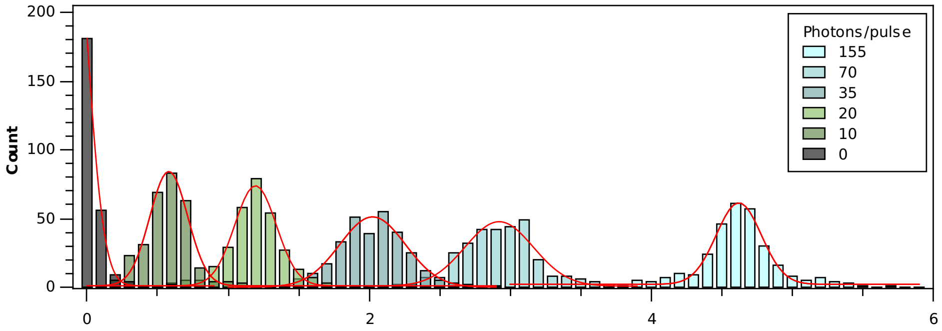

Figure 2.4: Counting histogram of peak response in arbitrary units for different photon numbers, data published in [4].

The BER for a distribution corresponding to a particular number of photons per pulse is calculated from the counting histogram as

$$BER = \frac{1}{2}\left[P_{1|0} + P_{0|1}\right] \tag{2.9}$$

where $P_{1|0}$ is the probability of registering a detection event in the absence of illumination, and $P_{0|1}$ is the probability of failing to register a detection event when illuminated by a pulse. Both probabilities can be found using the area overlap between the dark distribution and light distribution, whose Gaussian curves intersect in one point, called the decision point, ς

$$P_{1|0} = \frac{1}{2\pi{\sigma_0}^2}\int_{\varsigma}^{\infty} e^{-\frac{x^2}{2\sigma_0}}\,dx \tag{2.10}$$

$$P_{0|1} = \frac{1}{2\pi{\sigma_1}^2}\int_{-\infty}^{\varsigma} e^{-\frac{(x-\mu_1)^2}{2\sigma_0}}\,dx \tag{2.11}$$

where σ_0 and σ_1 are the standard deviations of the light-off and light-on distributions, respectively, and μ_1 is the mean of the light on distribution. After evaluation of the integrals, the probabilities come out to be

$$P_{1|0} = \frac{1}{2}\left[1 - erf\left(\frac{\varsigma}{\sqrt{2}\sigma_0}\right)\right] \tag{2.12}$$

$$P_{0|1} = \frac{1}{2}\left[1 + erf\left(\frac{\varsigma - \mu_1}{\sqrt{2}\sigma_1}\right)\right] \tag{2.13}$$

By choosing an optimal decision point, the BER can be simplified to

$$BER = \frac{1}{2} erfc\left(\frac{Q}{\sqrt{2}}\right) \tag{2.14a}$$

$$Q = \frac{\sigma_0\mu_1 + \sigma_1\mu_0}{\sigma_0 + \sigma_1} \tag{2.15b}$$

The resulting BER as a function of input photons per pulse is shown in Fig. 2.5.

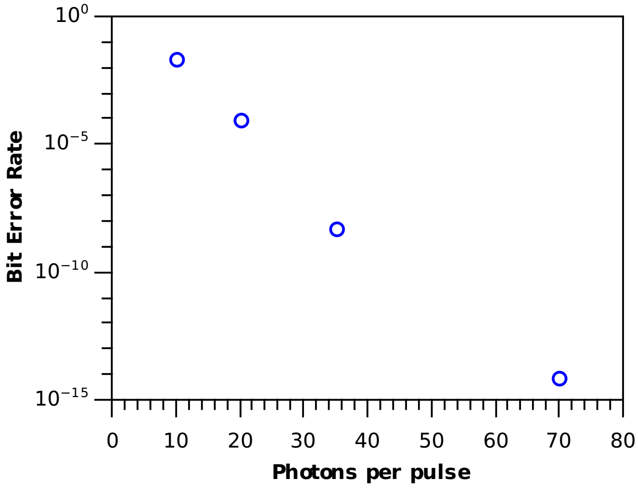

Figure 2.5: Bit error rate (BER) as a function of input photons per puse, data published in [4].

It is often useful to compare the detector sensitivity to that of an ideal noiseless detector limited only by Poisson statistics:

$$P(n,k) = \frac{n^k e^{-n}}{k!} \tag{2.15}$$

This corresponds to the probability of detecting k photons when the mean photon arrival is n photons. Thus, in an ideal noiseless detector, $P_{1|0} = \frac{0^k e^{-0}}{k!} = 0$ and $P_{0|1} = \frac{n^0 e^{-n}}{0!} = e^{-n}$. Thus, by equation (2.1),

$$BER = \frac{1}{2} e^{-n} \tag{2.16}$$

This means that if a detector is required to operate at a certain BER, equation (2.16) dictates the minimum number of photons the detector must be capable of detecting in order to achieve that BER. This is referred to as the quantum limit of photodetection. By inspection of Fig. 2.4, a BER of 0.01 is achieved at the maximum sensitivity of 10 photons per pulse. Using equation (2.7), a BER of 0.01 corresponds to a detection threshold of 6 photons. Thus, the MAGIC detector, having achieved this BER with 10 photons, is only 4 photons away from the quantum limit of photodetection.

2.4.4 MAGIC Detector Monte Carlo Model

To verify the advantages of the MAGIC detector over conventional single photon avalanche detectors, a Monte Carlo model is developed [7]. The model flowchart is shown in Fig. 2.6. A certain number of carriers are injected into the multiplication region at time t=0. The avalanche probability is calculated based on the local electric field and assumes saturation velocity of carriers. The avalanche probability is compared to a randomly generated lucky number for each charge carrier to determine whether that carrier initiates impact ionization. Hole escape probability and electron injection probability are two additional stochastic parameters introduced into the model. Carriers which exit either end of the multiplication region are removed from the simulation, and carriers which initiate impact ionization add charge carriers to the simulation. Additionally, the charge is sampled at the hole barrier to determine the degree of electron injection, which may also add electrons into the simulation through electron injection. The simulation is complete when there are no charge carriers remaining in the multiplication region. The simulation is run 500 times to get mean values for the peak current, from which SPDE can be calculated.

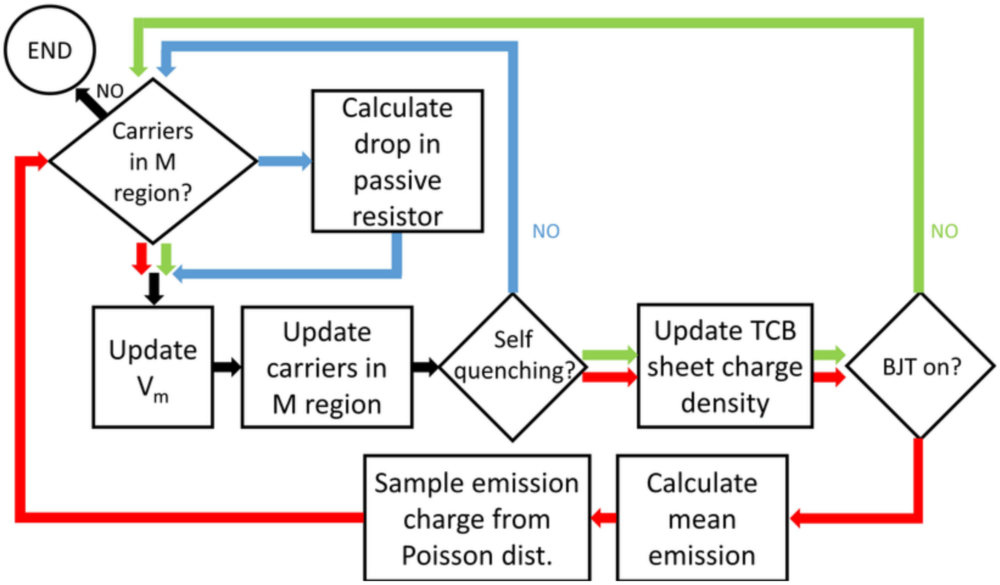

Figure 2.6: Flowchart for Monte Carlo simulation of MAGIC detector, from [8].

The MAGIC detector mean current as a function of photon number is shown in Fig. 2.7 for different conditions of emitter doping level and emitter conduction band offset. The MAGIC detector shows a dynamic range of almost two orders of magnitude from the single photon level up to 25 photons. The doping level and the conduction band offset of the emitter are the two model parameters that will determine the device stability. The condition of 5E19 cm^{-3} doping level and 375 meV conduction band offset for the emitter correspond to an unstable mode of operation for the device, seen from Fig. 2.7. By contrast, both self-quenched and passively quenched single photon avalanche detectors that do not use bipolar gain were found to have no linearity in this input range [7].

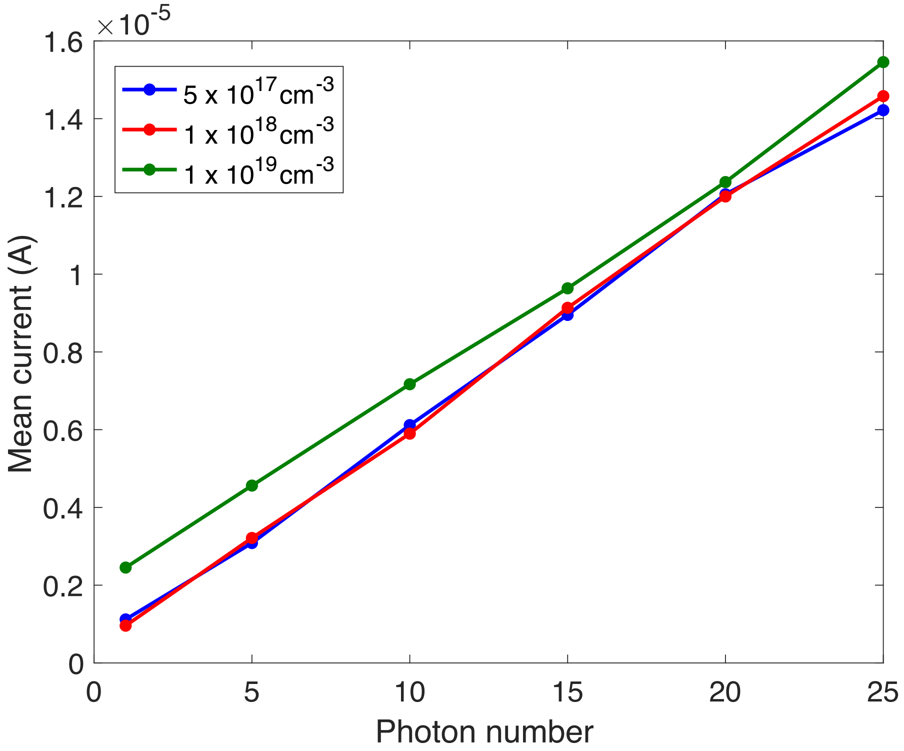

Figure 2.7: Mean peak current as a function of photon number for different conditions of emitter doping and emitter conduction band offset.

The SPDE of the MAGIC detector as a function of emitter conduction band offset for different emitter doping levels is shown in Fig. 2.8. The emitter doping and conduction band offset define a stability region for the device operation. The MAGIC detector is capable of achieving over 90% SPDE, which is significantly higher than achieved using self-quenched and passively quenched detectors without bipolar gain [7].

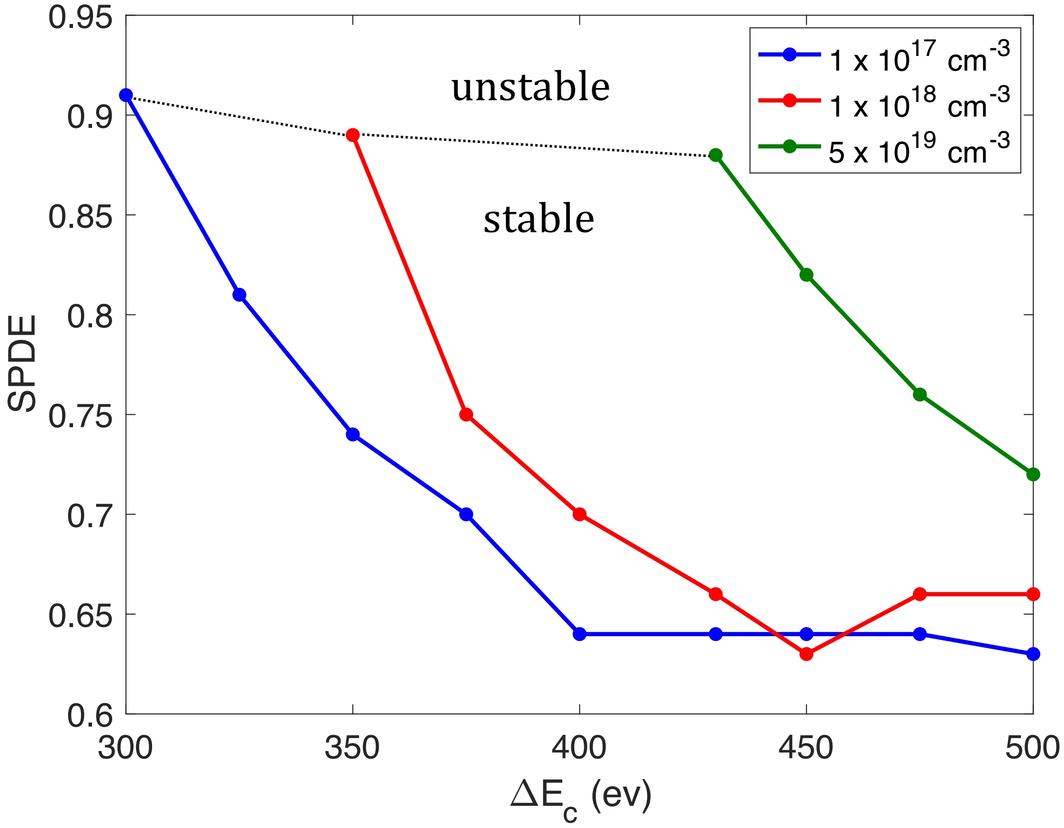

Figure 2.8: MAGIC detector SPDE as a function of emitter conduction band offset for different emitter doping levels.

2.5 Conclusion

Multiple Amplification and Gain with Internal Control (MAGIC) is a novel device concept that incorporates avalanche and bipolar gains in a single device. A one-dimensional model based on current continuity was used to optimize the strengths of avalanche and bipolar gains, where it was found that a τ_p/τ_n ratio between 0.01 and 0.001 is optimal. A MAGIC detector was realized, using bandgap engineering to modulate the bipolar and multiplication gains. The detector achieved a sensitivity of 10 photons with BER of around 10^{-2}, and a sensitivity of 35 photons at a BER of 5×10^{-9}. A Monte Carlo model based on the statistics of impact ionization, hole escape, and electron emission was developed, which showed single photon capability with high dynamic range and SPDE of over 90%.

Portions of Chapter 2 have been published in the following publications: S. N. Rahman, D. Hall, Z. Mei, and Y. H. Lo, "Integrated 1550 nm photoreceiver with built-in amplification and feedback mechanisms," Optics Letters 38, 20 (2015); S. N. Rahman, D. Hall, Z. Mei, and Y. H. Lo, "Multiple gain mechanisms integrated in APDs biased below breakdown for sensitivity improvement," Proceedings of the SPIE 8727, 87270P-1 (2013); D. Hall, Y. H. Liu, and Y. H. Lo, "Single photon avalanche detectors: prospects of new quenching and gain mechanisms," Nanophotonics 4, pp. 397-412 (2015). The dissertation author was the second author/primary investigator and author of these papers.

References:

1. D. A. Shushakov, and V. E. Shubin, “New solid state photomuultiplier,” Proceedings of SPIE 2397 (1995).

2. M. A. Itzler, X. Jiang, B. Nyman, and K. Slomkowski, “InP-based negative feedback avalanche diodes,” Proceedings of the SPIE 7222, Quantum Sensing and Nanophotonic Devices VI, 72221K, 2009.

3. S. N. Rahman, D. Hall, Z. Mei, and Y.H. Lo, “Integrated 1550 nm photoreceiver with built-in amplification and feedback mechanisms,” Optics Letters **38**, 20, pp. 4166-4169 (2013).

4. S.N. Rahman, D. Hall, Z. Mei, and Y.H. Lo, “Multiple gain mechanisms integrated in APDs biased below breakdown for sensitivity improvement,” Proceedings of SPIE 8727 (2013).

5. S. Adachi, *Properties of semiconductor alloys: group-IV, III-V and II-VI semiconductors*. Chichester, U.K.: Wiley, 2009.

6. X. H. Zhang, S. J. Chua, S. J. Xu, W. J. Fan, “Band offsets at the InAlGaAs/InAlAs (001) heterostructures lattice matched to InP substrate,” Journal of Applied Physics **83**, 5852 (1998).

7. S. N. Rahman, D. Hall, and Y. H. Lo, “Non-geiger mode single photon detector with multiple amplification and gain control mechanisms,” Journal of Applied Physics **115**, 173104 (2014).

8. D. Hall, Y. H. Liu, and Y. H. Lo, “Single photon avalanche detectors: prospects of new quenching and gain mechanisms,” Nanophotonics **4**, pp. 397-412 (2015).

Chapter 3 Carrier Multiplication through Disordered Materials

While one approach to mitigate the adverse effects of impact ionization is to limit the reliance upon impact ionization by using multiple gain mechanisms, another approach is to seek an alternative carrier multiplication mechanism. The approach taken here is to use disordered materials. Disordered materials feature either a disruption or elimination of the periodicity of the lattice, offering new physical properties. The result of utilizing disordered materials is a carrier multiplication mechanism which bears resemblance to impact ionization in that the mechanism is hot carrier-initiated, but holds unique characteristics. This carrier multiplication mechanism is called Cycling Excitation Processes (CEP) [1].

Whereas impact ionization involves extended states, or traveling Bloch waves, carrier multiplication involving disordered materials uses both extended and localized states. Hence, the localization of states seen in disordered materials relax the requirement of momentum conservation for the occurrence of carrier excitation to the mobile band. Silicon devices with internal gain based on impurity states have been developed [2] but require very low temperature operation to suppress thermalization of carriers from impurities and have slow operation due to slow relaxation of ionized impurities. Carrier multiplication based on impact ionization and carrier multiplication based on CEP both involve a reverse Auger process of a hot carrier transferring energy to excite either a secondary carrier or electron-hole pair to the mobile bands. Since the secondary carrier is excited from a localized state in the case of CEP, it is necessary to repopulate those localized states, which can be done through phonon excitation. Thus phonon dynamics become an important tool to modulate the gain and excess noise of carrier multiplication in disordered materials.

3.1 Background of Cycling Excitation Processes

For any internal gain mechanism based on carrier multiplication, it is important to consider the probability of carrier excitation for both electrons and holes since that probability determines both the achievable gain and also the excess noise of the device. As discussed previously, the impact ionization probability is governed by the ionization coefficients for electrons and holes, which is the characteristic distance a carrier must travel before initiating impact ionization, and is related exponentially to the electric field in the multiplication region.

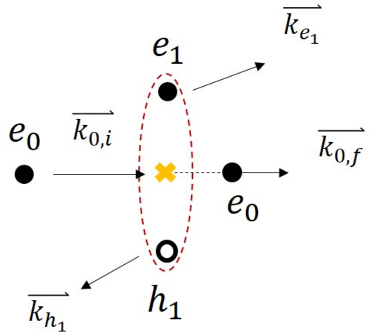

Figure 3.1: A schematic impact ionization collision.

While the impact ionization model introduced previously helps illustrate dependence of ionization probability on electric field and can be empirically fitted to experimental data, one can resort to conservation of energy and momentum to understand fundamental requirements of impact ionization.

Consider an initial electron e_0 with wavevector $\overline{k_{0,\iota}}$ and energy E_{0i}, which obtains a final wavevector $\overline{k_{0,f}}$ and energy E_{0f} by creating an electron hole pair through impact ionization, e_1 and h_1, with final energies and wavevectors E_{e1}, $\overline{k_{e1}}$, E_{h1}, and $\overline{k_{h1}}$, as in Fig. 3.1. Conservation of energy and momentum gives us

$$E_{0i} = E_{0f} + E_{e1} + E_{h1} + E_g = E_f \tag{3.1}$$

$$\overline{k_{0\iota}} = \overline{k_{0f}} + \overline{k_{e1}} + \overline{k_{h1}} = \overline{k_f} \tag{3.2}$$

Additionally, the final energy should be minimized for a given k$_f$, which stipulates that the group velocities of the final particles be the same [3]. Since the group velocity of an electron (hole) is proportional to the inverse effective mass of that carrier in the conduction (valence) band, we have $k_{0f} = k_{e1} = k_{h1}\frac{m_e}{m_h}$ and $k_f = k_{0f}\left(2 + \frac{m_h}{m_e}\right)$. We can rearrange eq. 1 to obtain

$$E_{0i} = \frac{\hbar^2 {k_{0f}}^2}{2m_e}\left(2 + \frac{m_h}{m_e}\right) + E_g \tag{3.3}$$

Furthermore, we can relate Eoi and koi as

$$E_{0i} = \frac{\hbar^2 {k_{0i}}^2}{2m_e} = \frac{\hbar^2}{2m_e}\left[k_{0f}\left(2 + \frac{m_h}{m_e}\right)\right]^2 = \frac{\hbar^2 {k_{0f}}^2}{2m_e}\left(2 + \frac{m_h}{m_e}\right)^2 \tag{3.4}$$

Equating equations (3.3) and (3.4), we obtain

$$E_{0i} = E_g\left(\frac{2+\frac{m_h}{m_e}}{1+\frac{m_h}{m_e}}\right) \tag{3.5}$$

When $m_h = m_e$, then the initial hot electron must have an energy equal to three halves the bandgap energy. For silicon, this corresponds to 1.8eV. While the above calculation corresponds to a simple two band approximation rather than three band case or other more realistic band cases, it gives a reasonable estimate of the required carrier energies involved in impact ionization and explains why silicon APDs typically require 50V to 200V reverse bias in order to satisfy both conservation of energy and momentum.

A carrier multiplication mechanism operating at low bias below 10V could be achieved if momentum conservation requirements could be relaxed. Shallow impurity levels have been shown to increase impact ionization probability [4]. We further propose that that the localization of states can enable an altogether new carrier multiplication mechanism. Impact ionization involves free carrier Bloch waves, which have uncertain positions but precise momenta. Due to the precision in momentum, the same conservation of momentum requirements discussed previously apply. Bound states, on the other hand, involve localization of states, and introduces uncertainty in momentum. Thus, momentum conservation, also called the k-selection rule, is more easily satisfied if bound states are involved in the carrier multiplication mechanism.

For indirect bandgap detectors such as silicon, momentum conservation requires that a particle of suitable k-vector be involved in the transition to account for the difference in k-space between the conduction band minimum and valence band maximum. In the case of extended states, only one k-vector can meet this criterion. For localized states, however, the imprecision in required k-vector makes this criterion much more easily satisfied, as shown in Fig. 3.2.

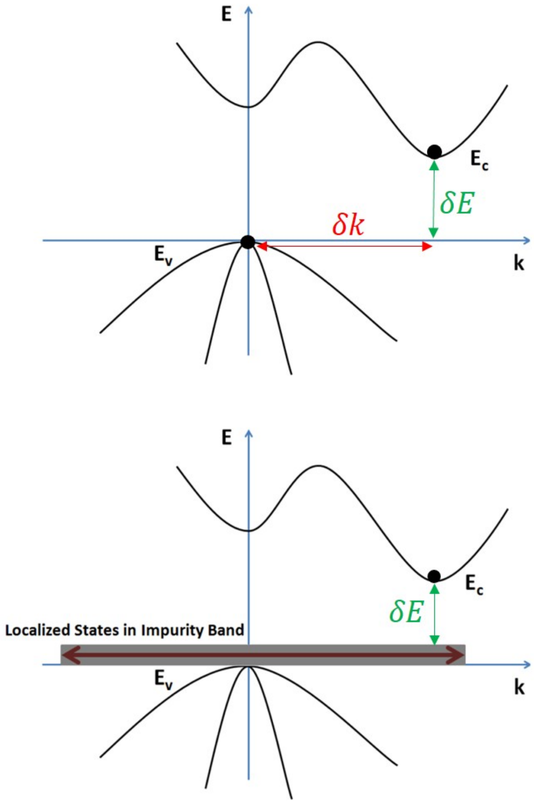

Figure 3.2: Energy versus momentum diagram for a band-to-band transition in an indirect bandgap semiconductor with and without localized states involved.

3.2 Auger Excitation

CEP involves two fundamental physical processes of Auger excitation of a charge carrier from a localized state to the mobile band, and phonon absorption to repopulate that localized state. These two processes complement each other in a cyclic process to facilitate carrier multiplication and yield a multiplication gain. These two processes, in connection with the localization of states discussed above, are outlined next.

The Auger effect is a process by which the energy released by an electron transitioning to fill a vacancy at a lower energy state in an atom can excite a different electron and eject it from the atom. In semiconductors, where discrete energy states from atoms in the lattice form quasi continuous energy bands, the Auger effect in semiconductors would result in the increase in energy of a charge carrier within the mobile band. For instance, Auger recombination is a process occurring in heavily doped semiconductors involving a free electron in the conduction band and a free hole in the valence band recombining across the bandgap. Auger recombination is distinguished from band to band recombination in that the energy released from the Auger recombination is transferred to another charge carrier to increase its energy. This could result in the increase in kinetic energy of a conduction band electron.

Thus, Auger recombination can be thought of as the reverse process of impact ionization, or equivalently, impact ionization as a reverse Auger effect. The type of reverse Auger effect used by CEP involves the excitation of a bound carrier to the mobile band by a hot carrier. Similar to impact ionization, the hot carrier releases some of its kinetic energy to excite an additional carrier to the mobile band. While the excitation in impact ionization is band-to-band, the excitation in CEP is from a bound state within the bandgap to the mobile band. The reverse Auger process involved in impact ionization results in three mobile carriers in the final state whereas the reverse

Auger process involved in CEP results in two mobile carriers in the final state. The third mobile carrier comes from the completion of the cycling process via phonon absorption, discussed in the next section.

Since Auger excitation leaves an impurity state unoccupied, an additional process is required to repopulate the vacant impurity state. This is done through electron-phonon interaction. An immobile electron, either a valence band electron or an electron bound to an impurity state within the bandgap, is excited by a phonon. This results in either an electron transition from the valence band to an available impurity state (for example a neutral acceptor), or from an impurity state (for example a neutral donor) to the conduction band. The former case involves the creation of a mobile hole in the valence band, while the latter case involves the creation of a mobile electron in the conduction band.

3.3 Phonon Absorption

Phonon absorption is the final step in the cycling process. The impurity that was neutralized in the Auger excitation is re-ionized by the absorption of a phonon. A free carrier is then created in the mobile band, in the opposite band as the free carrier generated in the Auger excitation. Thus, a free electron and free hole are created in the full cycling process.

Although in equilibrium, all minority impurities have been ionized by the majority impurities, CEP represents a dynamic process by which the hot carrier represents a perturbation. The neutralized acceptor has a significant probability to be re-ionized by phonon absorption rather than by a majority impurity due to the relative time scales; phonon interaction with carriers occurs on a time scale of ~1-100ps [5], and the localization of the impurity states increases the phonon coupling [6].

3.4 The Complete Cycle

The complete cycling process for a generic semiconducting material with localized states is shown in Figure 3.3. Note the band diagram may vary depending on how the localization is achieved. An electron from the p-region can become a hot electron by being accelerated by an electric field. After reaching a certain threshold energy, the hot electron can lose kinetic energy to excite a shallow localized electron in the n-region to the conduction band, as in Figure 3.3(a). Thus, the initial state consists of a hot electron and the final state consists of a cold electron and an additional free electron, both in the conduction band, and a localized hole. The localized state that lost an electron can regain an electron through phonon absorption, or coupling between the phonon and localized state. This phonon absorption process excites an electron from the conduction band in the n-region to that localized state, as in Figure 3.3(b), thereby leaving a mobile hole in the valence band. The initial state before the phonon absorption consists of the localized hole and the final state after the phonon absorption consists of the mobile hole in the valence band. The cycling process is complete, as that mobile hole can become accelerated across the gain region to become a hot hole. The cycling process can also occur with hot hole injection. The Auger excitation will then involve an electron in the valence band being excited to a shallow localized state in the p-region, Figure 3.3(c). The phonon absorption process involves the electron in that localized state to be excited to the conduction band, Figure 3.3(d).

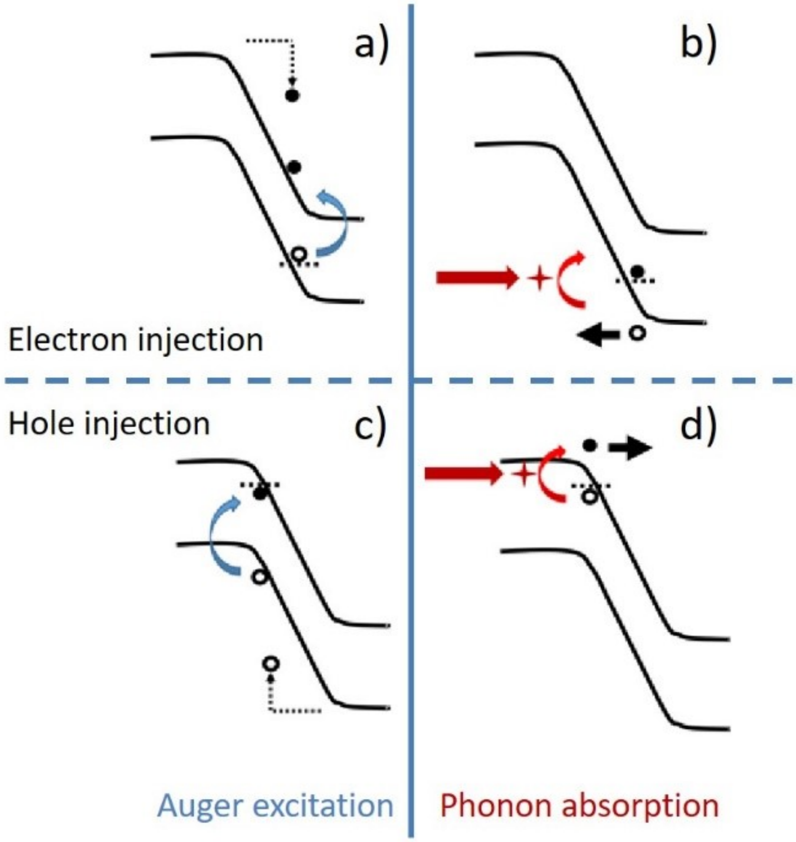

Figure 3.3: Illustration of Cycling Excitation Processes.

The cycling process can also be represented with Feynman diagrams, shown in Fig. 3.4, which depict the interactions as they occur chronologically through time. Each intersection on a Feynman diagram involves three lines. The lines with arrows represent fermions (e.g. electrons). and the third line represents a boson (e.g. photon or phonon). The intersection represents an interaction. A right pointing arrow represents an electron while a left pointing arrow represents a hole. A dashed line represents a Coulomb interaction, i.e. Auger excitation. A curvy line represents a phonon absorption. Initially at time t_0, there is a hot electron e_{hot}. After the Auger excitation at time t_1, there is a cold electron e_{cold}, an additional free electron in the conduction band e_n, and a localized hole h_{bn}. Finally, after the phonon absorption at time t_2, there is a free hole in the valence band h_n.

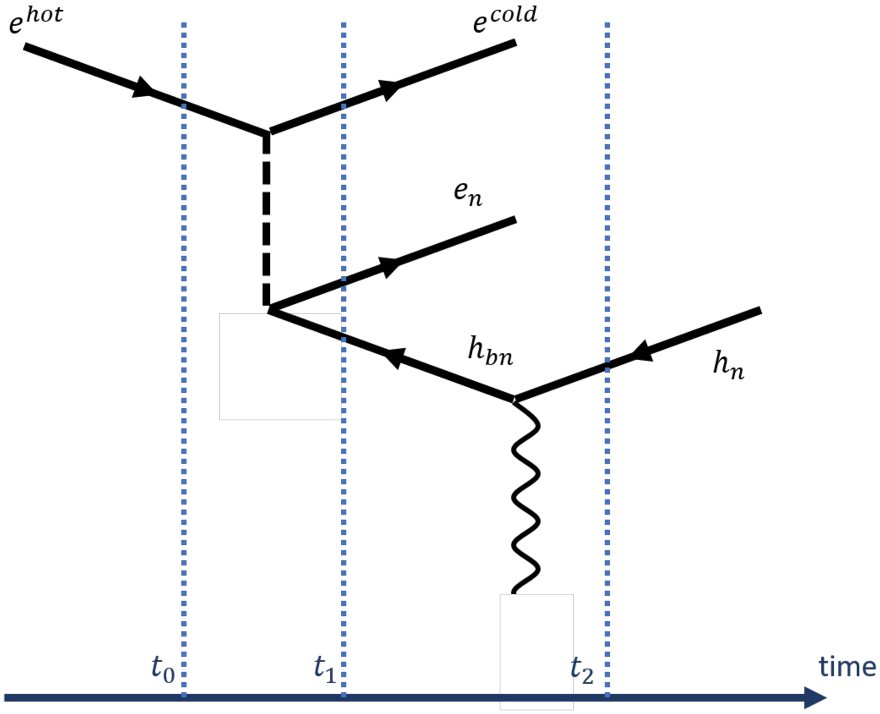

Figure 3.4: CEP represented with a Feynman diagram.

3.5 Conclusion

This chapter introduced Cycling Excitation Processes (CEP) as an alternative internal signal amplification mechanism to impact ionization. CEP uses disordered materials which introduce localized states that relax the k-selection rule of momentum conservation. CEP uses two key physical processes of Auger excitation and phonon absorption.

References:

1. Y. Zhou, Y. H. Liu, S. N. Rahman, D. Hall, L. J. Sham, and Y. H. Lo, “Discovery of a photoresponse amplification mechanism in compensated PN junctions,” Applied Physics Letters **106**, 031103 (2015).

2. J. Kim, K. S. McKay, M. G. Stapelbroek, and H. H. Hogue, “Opportunities for single photon detection using visible light photon counters,” Proceedings of the SPIE, 8033, 80330Q-1 (2011).

3. F. Capasso, Semiconductors and Semimetals. Semiconductors and Semimetals Vol. 22 Lightwave Communications Technology Part D Photodetectors, ed. W. T. Tsang, Academic Press Inc, Orlando 1985.

4. R. S. Crandall, “Impurity photoconductivity and impact ionization of shallow states in semiconductors, Journal of Applied Physics **42**, 3933 (1971).

5. J. Shah, *Ultrafast spectroscopy of semiconductors and semiconductor nanostructures*. Second enlarged edition, Springer, Berlin, 1999.

6. R. Atta-Flynn, P. Biswas, and D. A. Drabold, “Electron-phonon coupling is large for localized states,” Physical Review B **69**, 245204 (2004).

Chapter 4 Cycling Excitation Processes in a Heavily Doped Junciton

4.1 Physics of CEP in a Heavily Ddoped Junction

The first demonstration of CEP was in heavily doped and partially compensated silicon. A description of the doping profile is provided. The material is compensated on both sides of the p-n junction, with N_{Dn} and N_{An} being the donor and acceptor doping concentrations in the n-region, respectively, and N_{Dp} and N_{Ap} being the donor and acceptor doping concentrations in the p-region, respectively. $N_{Dn} > N_{An}$ and $N_{Ap} > N_{Dp}$. There exist ionized acceptors in the n-region, N_{An}^{-}, and ionized donors in the p-region, N_{Dp}^{+}, whose concentrations in equilibrium are roughly equal to the n-region acceptor concentration and p-region donor concentration, respectively. That is, the minority acceptors in the n-region completely ionize by accepting electrons from the majority donors and the minority donors in the p-region completely ionize by accepting electrons from the majority acceptors:

$$N_{An}^{-} = N_{An} \tag{4.1a}$$

$$N_{Dp}^{+} = N_{Dp} \tag{4.1b}$$

The majority donors in the n-region and majority acceptors in the p-region also ionize in this process. The remaining majority impurities after complete ionization of minority impurities will predominantly ionize by thermalization, adding a free carrier to the mobile band. Thus, the free carrier concentrations are given by:

$$n \cong n_n + n_p = (N_{Dn} - N_{An}) + (N_{Dp} - N_{Ap}) \tag{4.2a}$$

$$p \cong p_n + p_p = (N_{An} - N_{Dn}) + (N_{Ap} - N_{Dp}) \tag{4.2b}$$

Where n_n, n_p, p_n, p_p are the free electron and hole concentrations (denoted by main character) in the n and p regions (denoted by subscript). This means that the majority impurities also completely ionize, first by ionizing the minority impurities and next by free carrier thermalization:

$$N_{Ap}^{-} = N_{Dp} + p_p = N_{Ap} \tag{4.3a}$$

$$N_{Dn}^{+} = N_{An} + n_n = N_{Dn} \tag{4.3b}$$

However, it is the ionized minority ionized impurities N_{An}^{-} and N_{Dp}^{+} that are relevant to the CEP effect.

The complete cycling process for a heavily doped and partially compensated junction is shown in Fig. 4.1. The hot electron can, with a certain probability, release some of its kinetic energy to excite a localized acceptor-bound electron in the n-region into the conduction band via an Auger excitation process. This process neutralizes the minority acceptor in the n-region and results in a free electron in the conduction band (in addition to the original hot electron which becomes a “cold” electron after losing kinetic energy). The neutral acceptor has a vacancy and is capable of accepting an electron. By phonon absorption, involving an electron-phonon interaction, an electron can be excited from the valence band to the acceptor state, which re-ionizes the acceptor. The result is a free hole in the valence band. This free hole can be accelerated by drift across the depletion region and initiate an Auger excitation. The hole-initiated Auger excitation will neutralize a minority donor in the p-region and result in the creation of a free hole in the valence band. A phonon interaction with the localized electron can result in phonon absorption, by which the donor-bound electron is excited to the conduction band to become a free electron and the minority donor is re-ionized.

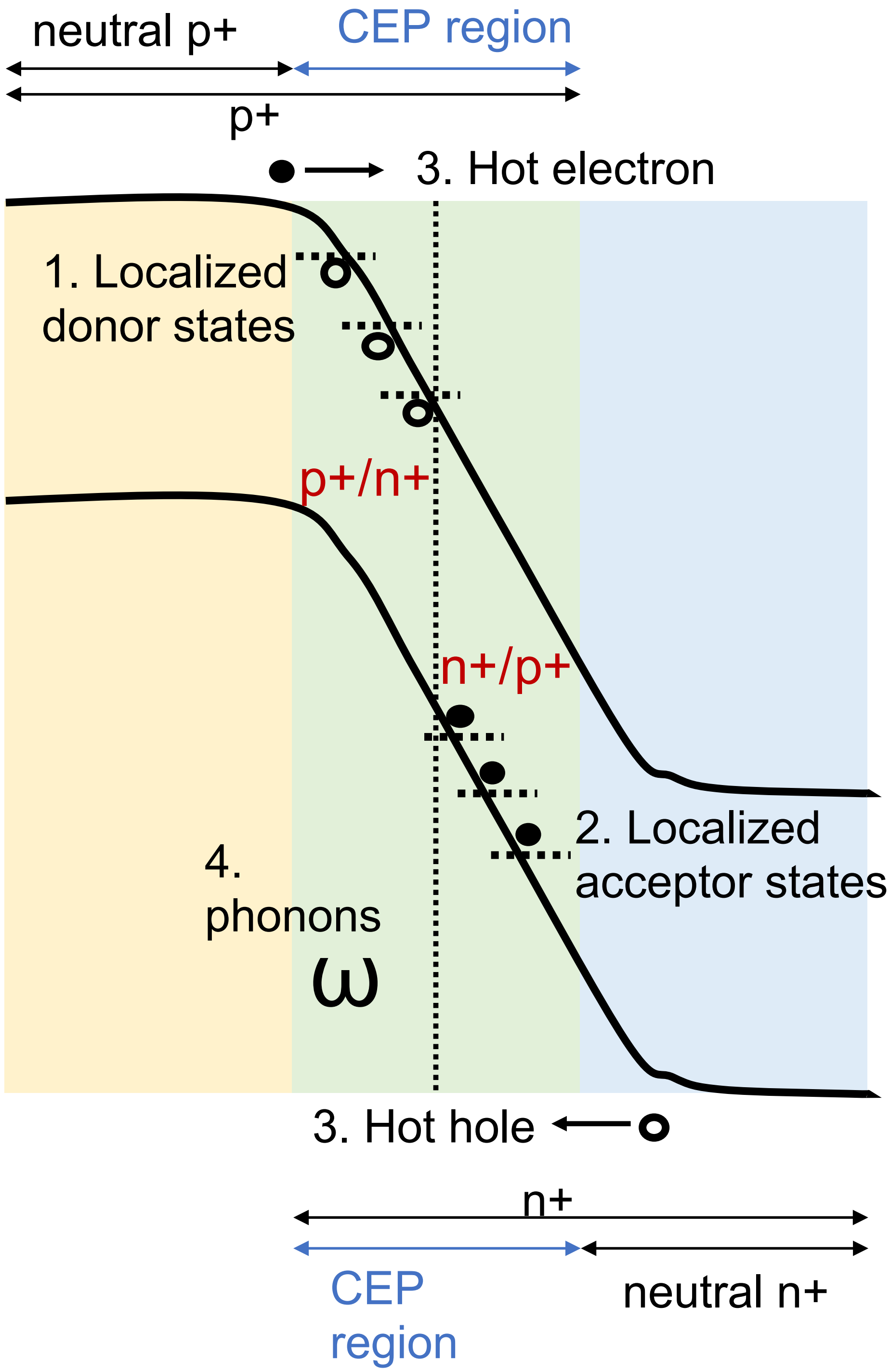

Figure 4.1: CEP in a heavily doped and partially compensated p-n junction.

4.2 CEP Detector Design

Based on the CEP principles discussed in the previous chapter, an epitaxial structure and device design must be implemented to create a working CEP-based detector. To realize the CEP detector, an epitaxial structure is grown by Metal-organic Chemical Vapor Deposition (MOCVD). This process can precisely control the dopant concentration, particularly important for the heavily doped and partially compensated CEP region. The epitaxial structure is shown in Table 4.1. The substrate is degenerately doped n-type. A 3um moderately doped n-type layer is grown on the substrate. Next, the CEP region is grown, which are the heavily doped and partially compensated n and p regions. Next, the moderately doped p-type layers are grown. Finally, a heavily doped p-type cap layer is grown as the top layer. The presence of localized boron impurities has been verified with Raman spectroscopy which shows B11 isotope and B10 isotope peaks at 620 cm^{-1} and 644 cm^{-1}, respectively. These boron isotope peaks are prevalent in samples with a heavily doped and compensated region but absent without, as shown in Fig. 4.2.

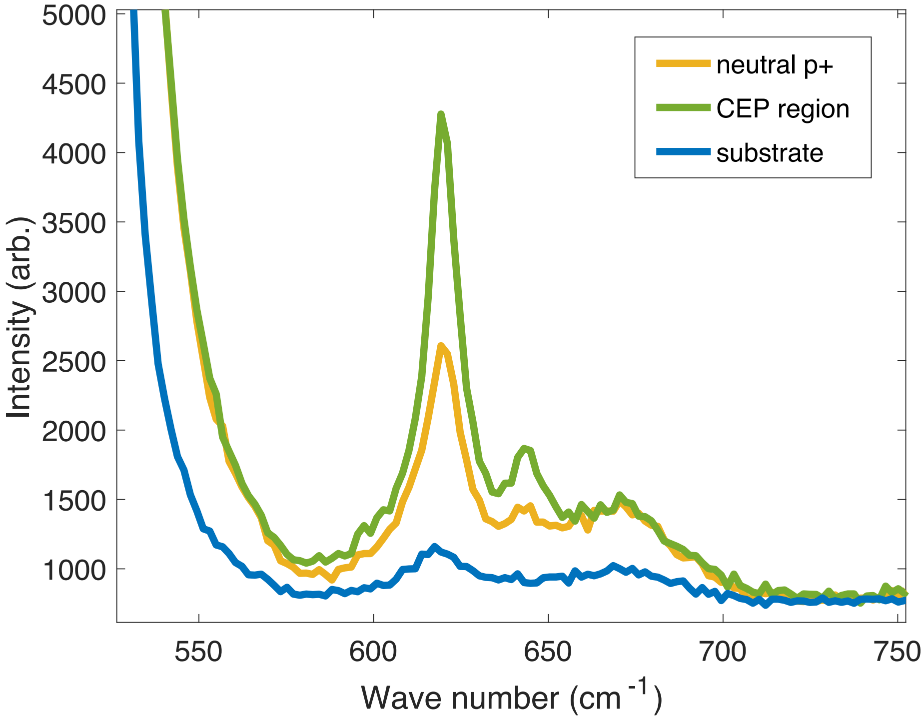

Figure 4.2: Raman spectrum of silicon samples with a neutral p+ region, CEP region, and n-type substrate.

Table 4.1. Epitaxial structure of the silicon CEP Detector.

Material	Thickness (um)	Doping (cm-3)
Si substrate		n++
Si	3.0	n=2E17
Si	0.1	n=2E18
Si	0.2	n=3E19, p=2E19
Si	0.2	P=3e19, n=2e19
Si	0.1	P=1e18
Si	0.15	P=2e17
Si	0.05	P=1e18

The fabrication process is shown in Fig. 4.3. A dry mesa etch is done using an Oxford Plasmalab P100 etcher, which defines the device active area by etching all epitaxial layers down to the substrate. Next, the sidewalls are passivated by deposition of silicon dioxide (SiO_2). Openings are etched in the SiO2 to allow contact to the top of the mesa (p-type cap layer) and the bottom of the mesa (n++ substrate). Indium metal is applied to the backside of the sample such that the bottom electrode contact could either be the at the bottom of the mesa or the back of the sample.

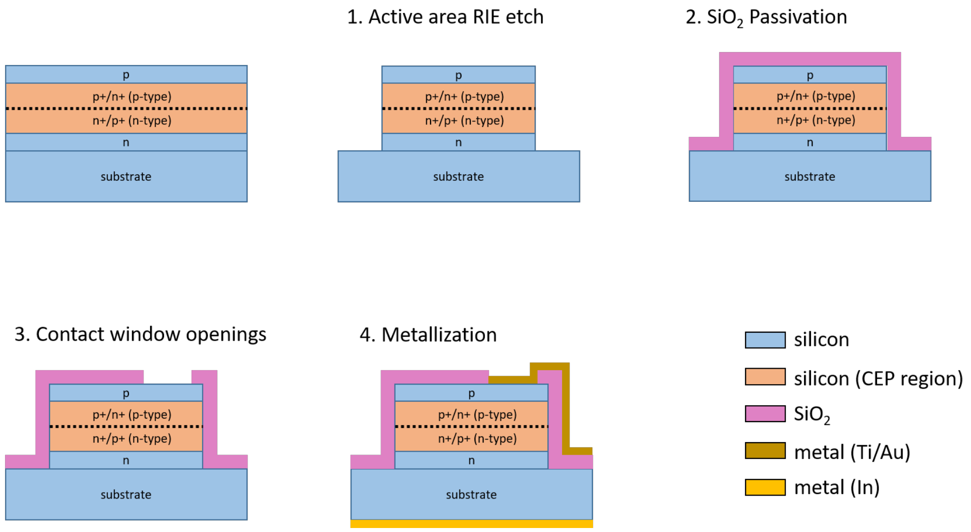

Figure 4.3: Device fabrication process flow for the heavily doped partially compensated CEP detector.

The final device schematic cross section is shown in Fig. 4.4(a). The total CEP region is 400nm to ensure light absorption in the CEP region for high quantum efficiency and also suitable thickness for high probability of carrier excitation via CEP. A micrograph of the top view of the device is shown in Fig. 4.4(b). The active area of the final device is a rectangular structure with dimension 35um x 55um.

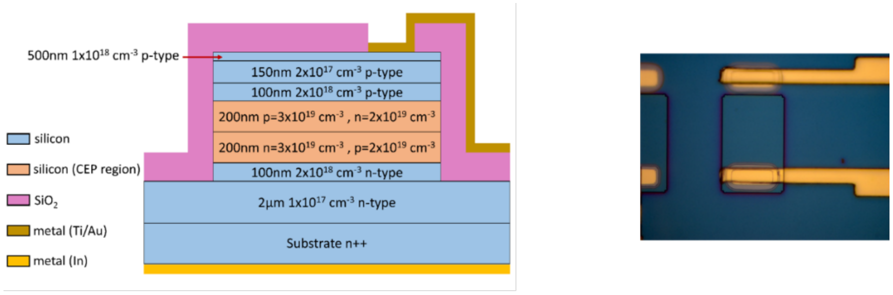

a) b)

Figure 4.4: The final device cross section schematic (a) and top view micrograph of the device active area (b).

4.3 Phonon Interactions in a CEP Device

CEP involves electron phonon interactions, and hence the phonon concentration is crucial to CEP operation. If the local phonon density of states is small compared to the hot carrier density, the Auger excitations vastly outnumber the available phonons to re-ionize the impurities that were neutralized during the Auger process. Since the phonon absorption process is necessary to complete the cycling process, there is a “phonon bottleneck” effect when the hot carrier density exceeds the local phonon density. The hot carrier density can be increased either by photogeneration of electron-hole pairs or by increasing the reverse bias voltage. The phonon bottleneck effect can be observed in both of these situations, where it is observed that this effect serves as a negative feedback mechanism that both favors high sensitivity and allows for low noise operation.

4.4 635 nm CEP Detector

Visible wavelength photodetectors are important for imaging and sensing, and the CEP detector is well-suited for high performance in the visible range. A CEP detector with the above epitaxial structure was measured at 635nm illumination [1]. The device is illuminated with a fiber coupled 635nm laser diode. A DC source meter is used to apply a bias and read the current. A Janis VPF-100 cryogenic chamber is optionally used if low temperature measurements are to be performed. Since the device does not exhibit a separate absorption multiplication region structure, there is no punch-through voltage that can be used as a unity gain reference. Thus, we take zero bias to be the unity-gain reference. The photocurrent is the difference between current under illumination and current in dark condition. The primary photocurrent is the photocurrent at unity gain, which we take to be zero bias. The gain at a given bias is then the ratio of the photocurrent at that bias to the primary photocurrent.

The DC current-volgate characteristics demonstrate rectifying behavior typical of a p-n junction. The gain versus bias for 635nm illumination is shown in Fig. 4.5. A maximum gain of over 4000 is achieved at around 3V reverse bias. For comparison, to achieve a gain of 10 to 100 in a silicon APD, the APD bias would need to be 20V to 100V. The high gain at low bias is a feature that makes CEP a promising alternative to impact ionization. Another beneficial feature of CEP is the negative feedback that favors low input light conditions and low noise operation.

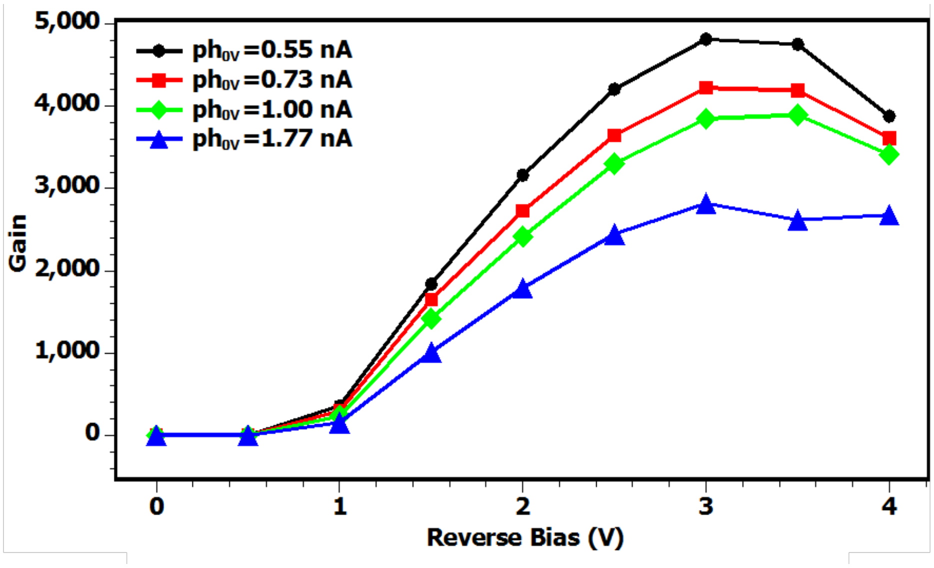

Figure 4.5: DC Gain versus reverse bias voltage for the CEP detector at 635 nm wavelength, from [1].

First, for a given bias voltage, the gain increases with decreasing input light power. This can be seen in Fig. 4.5, where the primary photocurrent is directly proportional to the input light power. The highest gain is achieved for 0.55nA primary photocurrent, which was the smallest primary photocurrent used for gain characterization. This results from the negative feedback phenomenon, related to hot carrier concentration with respect to the local phonon density. Under high light conditions, there is a larger density of hot carriers and hence a larger density of Auger excitations. In order to maximize the CEP gain, the number of Auger excitations should be in proportion to the local phonon density of states. Under high input optical illumination, however, the number of Auger excitations exceeds the local phonon density. Hence, there is diminishing return in the form of photocurrent as the optical power is increased. This effect favors low input light level conditions for device operation and is promising for single photon capability of a CEP detector.

Negative feedback is also manifested in the gain saturation beyond 3V reverse bias, also shown in Fig. 4.5. Just as increasing the input optical power will increase the hot carrier concentration though photogeneration, increasing the reverse bias voltage will increase the hot carrier concentration by increasing the electric field across the CEP region and accelerating carriers to greater kinetic energies on average. In avalanche detectors, on the other hand, the gain continues to increase with increasing bias beyond the avalanche breakdown voltage and eventually diverges. The gain close to the operating bias varies drastically with even a slight change in bias. Avalanche detectors thus require a quenching mechanism, either in the form of an active quenching circuit, passive resistive layer, or bandgap engineering to reduce the electric field across the multiplication region as the avalanche charge builds up. For a CEP detector, the negative feedback inherent in the balance between hot carriers and phonons results in a stable gain at the operation bias.

To verify the role of electron-phonon interaction in the CEP effect, the temperature dependence of the gain was also studied. Fig 4.6 shows the normalized gain versus reverse bias voltage for different temperatures between 140K and 300K. The gain decreases markedly with decreasing temperature. This arises because phonons follow Bose-Einstein statistics, which stipulate that there is no limit to how many bosonic particles can occupy a given energy state, and the probability of occupation at a given energy increases with temperature. In avalanche based detectors, higher temperatures increase the breakdown voltage required for impact ionization as a result of electron phonon scattering, meaning that at a given bias, the gain decreases with increasing temperature. In CEP based detectors, however, the gain increases with increasing temperature, indicating that phonons are essential for CEP.

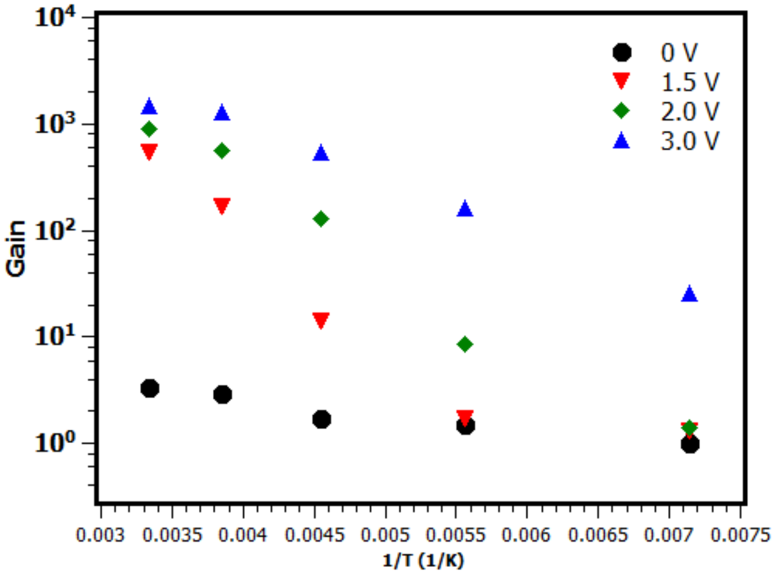

Figure 4.6: Gain dependence on temperature, from [1].

4.5 CEP Noise Characteristics

An additional result of negative feedback is a reduction of gain fluctuation. This was observed in the MAGIC detector device and was made possible by the incorporation of coupled gain mechanisms, namely avalanche gain and bipolar gain, which counterbalanced each other. Gain regulation through negative feedback is accomplished in a CEP detector by coupled Auger excitations and electron-phonon interactions. Just as in the MAGIC detector it was necessary to optimize the device operation and ensure a suitable balance between avalanche and bipolar gain through bandgap engineering, in the CEP detector it is necessary to ensure that Auger excitation and photon absorption processes are balanced through engineering of disorder. In this case, engineering of disorder occurs through the doping level and degree of compensation through precise doping profile.

4.5.1 Noise Measurement Background

To demonstrate that negative feedback results in low-noise operation, it is necessary to perform a noise characterization experimentally. The complete noise analysis of the CEP detector requires the measurement of the excess noise factor as a function of multiplication gain. This first involved determining the multiplication gain as a function of bias through a DC measurement. Next, the noise power at a suitable frequency as a function of bias must be measured. In some photodiode setups, the device is illuminated with a modulated (e.g. chopped) light source and the photocurrent and multiplication noise are measured from a lock-in amplifier [2]. The noise measurement performed on the CEP detectors, however, involved separate measurements for the DC multiplication gain and noise power bias dependence at a certain frequency.

Measuring the DC gain as a function of bias requires knowledge of the bias at which the gain is equal to 1, or the unity gain bias. Whereas in Reach-through APD's the unity gain bias is well-defined by the punch-through voltage at which the electric field penetrates into the absorption region, the CEP detectors utilize an all-silicon design and have no punch-through voltage. However, we can take the unity gain bias to be zero bias. The photocurrent gain at a given bias is then defined as the ratio of the photocurrent at that bias to the zero bias photocurrent.

4.5.2 Noise Measurement Procedure

Measuring the excess noise factor requires a measurement of the noise power spectrum. One common way to measure the noise power is to use a Noise Figure Meter [3], which measures the device noise figure, defined as the ratio of the input SNR to output SNR. The input SNR would be determined by calibration with a pre-determined noise source at the input of the device. The device would then be placed in series with the noise source, and the device output measured with the noise figure meter. Since noise figure meters are commonly used to measure two-port devices and photodiodes are one-port devices, rather than use a noise source for calibration, the photodiode measurement in dark condition would be used as the calibration. In this configuration, the measurement could equivalently be performed with a spectrum analyzer [4], which is the method that was chosen for the CEP detectors. For a measurement of the CEP detectors with a Spectrum Analyzer, the noise power spectrum in dBm/Hz of the device is obtained. A spectrum analyzer will take the fast Fourier transform of the input signal over a certain frequency bandwidth. The power in Watts can then be calculated as $P(W) = 10^{\frac{(p(dBm)-30)}{10}}$.

The challenge of noise power measurements is to measure the noise power at as low of a multiplication gain as possible, ideally unity gain. If this is possible, then the exact excess noise factor can be determined. Consider the noise power at unity gain, P_o, where M and F are 1: $P_o = 2e(I_{do} + I_{pho})M^2FBR = 2e(I_{do} + I_{pho})BR$. P_o and I_{pho} are related linearly by the proportionality constant 2eR. If it is desired to determine P_o for devices without a punch-through voltage, it can be done so by measuring the noise power at unity-gain under different optical input power and hence different primary photocurrent I_{pho} to determine this proportionality constant [5]. This same technique can also be applied at low multiplication gain close to unity gain [6]. The noise power at a higher gain is then given by

$$P = P_o M^2 F \tag{4.4}$$

If it is not possible to measure the noise power at unity gain, only relative excess noise factor and not the exact excess noise factor can be determined. The relative noise power from measurements performed at two different bias voltages V_1 and V_2 at a constant input optical power is given by

$$\frac{F(V_2)M^2(V_2)}{F(V_1)M^2(V_1)} = \frac{P(V_2)}{P(V_1)} \tag{4.5}$$

Where V_1 is taken to be the voltage at which the smallest possible noise power can be measured, and V_2 is some higher voltage. If $P(V_1) = P(V_o)$, then equation (4.4) is recovered. Although the exact excess noise factor cannot be determined if $P(V_1) > P(V_o)$, the excess noise of the CEP device can readily be compared to that of APDs.

It is important to know the sensitivity of the measurement setup as this will determine the smallest noise that can be measured. First, the noise figure of the HP 8594E spectrum analyzer used in the measurement is 24dB. Additionally, a low noise amplifier (LNA) was used further reduce the system noise floor. The LNA had a noise figure of 1.8dB and a power gain of 28.2dB. The noise factor of the system can be calculated by Friss' Formula as

$$F_{cascaded} = F_{LNA} + \frac{F_{analyzer-1}}{G_{LNA}} = 1.51 + \frac{251-1}{661} = 1.89 \tag{4.6}$$

The system noise figure is then $10\log 1.89 = 2.76dB$. The LNA improves the noise floor from -174dBm/Hz to -171.2dBm/Hz based on $-\frac{174dBm}{Hz} + 2.76dB = -171.2dBm/Hz$. Another way of expressing the utility of the LNA is that the LNA improves the noise figure of the system from 24dB to 2.76dB.

The setup used to measure the excess noise of the CEP detector is shown in Fig. 4.7. The device under test (DUT) is illuminated with a 635nm continuous wave (CW) laser. The DUT is packaged in a chip carrier with top and back electrodes wire-bonded to the package pins, which are then soldered to an SMA connector. The output of the device is passed into a bias-T. A bias is applied to the device using a Keithley 2400 through the inductive port of the bias-T. The noise of the device then passes through the capacitive port of the bias T, which is connected to an LNA. A 50 Ohm resistor was also placed between the bias-T and the LNA in order to provide appropriate impedance matching to a 50 Ohm environment. Finally, the output of the LNA is passed to the input of an HP 8549E Spectrum analyzer. The noise power was measured at 70MHz to avoid low frequency 1/f noise.

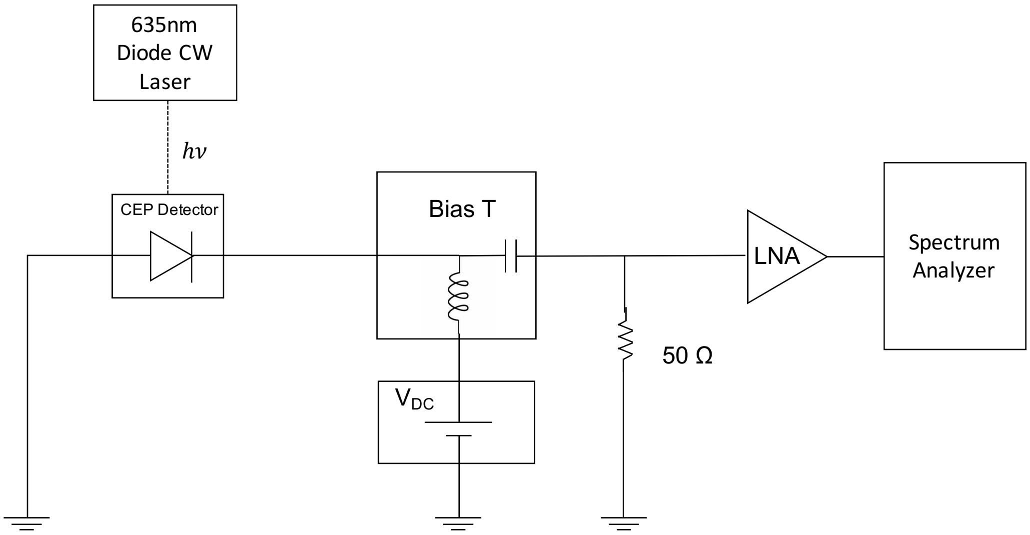

Figure 4.7: Noise measurement experimental setup.

4.5.3 Noise Measurement Calibration

The noise measurement setup described above was first calibrated with an Advanced Photonix (APX) high speed small area silicon APD, part number 012-70-62-54, at 635nm wavelength. The light and dark current was measured as a function of bias by performing a DC sweep using the Keithely 2400 DC source meter. The photocurrent is the difference between the light and dark currents, and the gain taken to be the ratio of photocurrent at a given bias to the zero-bias photocurrent. The resulting avalanche multiplication gain as a function of reverse bias voltage is shown in Fig. 4.8.

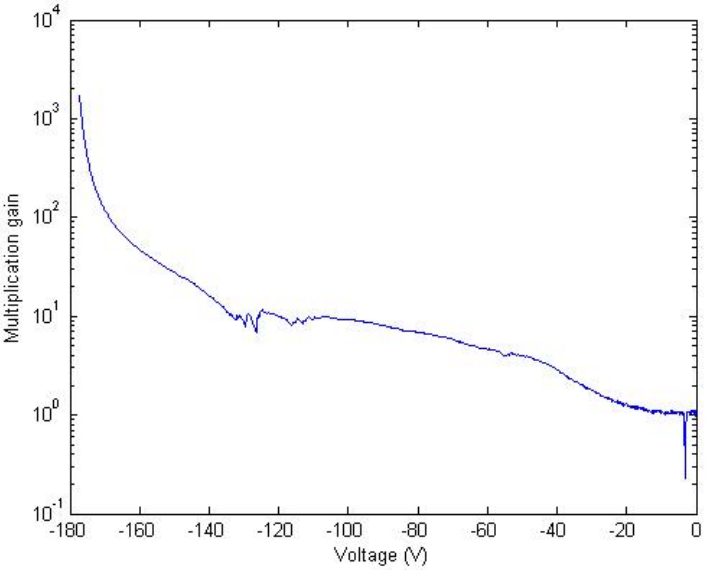

Figure 4.8: Multiplication gain versus voltage for the Advanced Photonix APD used for noise setup calibration.

The noise power at 70MHz at different bias was measured in the light and dark for the commercial APD for a wide range of multiplication gains. The power in dBm/Hz was converted to linear, the dark power subtracted, and the resulting data adjusted based on the noise floor and the LNA chain. Since the gain versus bias data contains thousands of data points whereas the noise power versus bias data contain a much fewer number of data points, interpolation was used in order to obtain the noise power versus multiplication gain from these two differently-sized data sets. The noise power versus multiplication gain data set was made to be the same size as the noise power versus bias data set. Since the noise floor was not low enough to measure the noise power at unity multiplication gain, as explained previously, a suitable scaling factor was chosen to satisfy McIntyre's Model for silicon, where k=0.02, based on the ratio of the noise power at a given bias to the smallest measurable noise power. The excess noise factor of the APX commercial detector is plotted in Fig. 4.9, along with a fit for McIntyre's Model for silicon. The good fit indicates that the experimental setup for measuring noise power and the procedure for extracting excess noise factor works well.

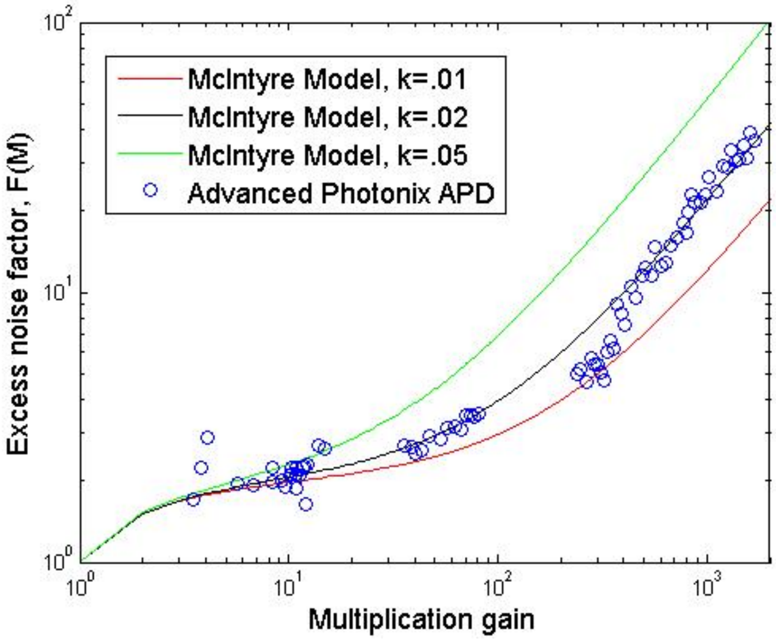

Figure 4.9: Excess noise factor as a function of multiplication gain for the Advanced Photronix APD, fitted with McIntyre's model.

4.5.4 Excess Noise Factor of the CEP Detector

The noise power of the CEP detector described previously in this chapter was measured using the same process described above, also measured for 635nm wavelength. The excess noise of the CEP detector as a function of gain is shown in Fig. 4.10, along with the excess noise factor of the APX commercial silicon APD and

McIntyre's model fit for silicon. The noise power of the CEP detector was below the -171 dBm/Hz noise foor. Thus, the CEP excess noise factor plotted in Fig. 4.10 represents the upper limit of excess noise, calculated as $2eI_{ph0}G^2F(G) \leq 171\ dBm/Hz$, where G is the excess noise factor of CEP. The CEP excess noise factor is 1.33 at a gain of 2419. At the same gain, this corresponds to about 30 times lower than the excess noise of a silicon APD. It should also be noted that for an ideal APD corresponding to k=0, McIntyre's model results in an excess noise factor of 2, as shown in the introduction. Thus, the CEP based all-silicon detector is capable of surpassing the fundamental noise limits of APDs, which for decades have served as the detector of choice for optical fiber communications.

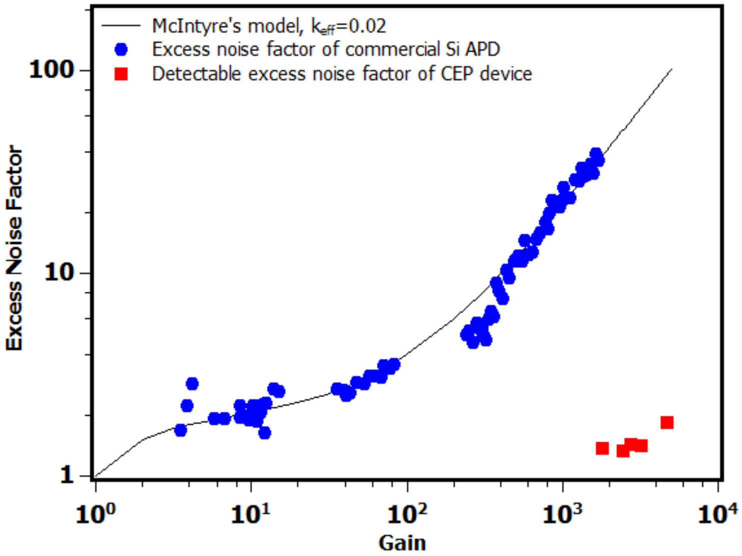

Figure 4.10: Excess noise factor of the commercial silicon APD fitted with McIntyre's model, and detectable excess noise factor of the CEP device, from [1].

4.6 1060 nm CEP Detector

4.6.1 Overview of 1060 nm Detection in Silicon

While visible wavelength detection in silicon based materials is natural due to the high absorption coefficient in silicon of visible wavelength light, detection in the near infrared in silicon remains a challenge. The bandgap of 1.12eV in silicon corresponds to a wavelength of 1100nm. Beyond 1100 nm wavelength there is a sharp decline in the absorption coefficient in silicon. This is because in classical detectors, a phonon with energy of at least the semiconductor bandgap energy is required for photogeneration of an electron-hole pair. Even near infrared wavelengths close to but below 1100nm still suffer from a relatively small absorption coefficient compared to visible wavelengths.

Photodetectors sensitive to infrared wavelengths are important for fiber optic communications, where the 1310nm and 1550nm bands are preferred due to low dispersion loss. Additionally, there are applications for near infrared wavelengths such as 1060nm. The 1060nm wavelength is important for free space communications for security systems. The 1060nm wavelength is also important in the field of medicine, for example surgical methods and medical laser treatments [7, 8]. 1060nm is important in materials processing [9]. Finally, 1060nm is used for defense applications [10] including rangefinding techniques such as LIDAR.

Based on the silicon absorption coefficient, roughly 600um would be needed to achieve acceptable quantum efficiency in a conventional photodiode. 600um, being a standard silicon wafer thickness, far exceeds a desirable device thickness. Many techniques of achieving high responsivity at 1060nm in an all-silicon detector without using an exceedingly thick silicon absorption layer have been applied. One common technique micromachining by pulsed lasers to form silicon microstructures [11-15]. Another type of device is a microdischarge device [16]. Finally, porous silicon devices have achieved appreciable responsivity [17-20]. However, these techniques are ultimately not capable of producing scalable, CMOS compatible single photon sensitivity since they either rely on photoconductive gain, use processes not CMOS compatible, or utilize surface states to enhance light absorption. Absorption by defect states results in larger flicker noise than by band-to-band absorption. Also, photoconductive devices have large dark current as well as generation and recombination noise. We demonstrate that by incorporating CEP into a photodiode, high responsivity and high gain at 1060nm can be achieved at low operation bias.

4.6.2 1060 nm CEP detector Experimental Results

The detector used for 1060nm detection [21] has the same epitaxial structure and device design as described previously for the 635nm CEP detector. The photocurrent and gain are also defined in the same way. The measurement setup is shown and is similar to that used for the 635nm setup, with the exceptions being that the optical source is a free-space coupled PiLAS Advanced Laser Diode Systems 1060nm laser diode and there is no cryogenic chamber since only room temperature characterization was performed for 1060nm illumination. The reverse bias dark current is plotted in Fig. 4.11, showing roughly 1uA of dark current at 4V reverse bias, as well as the reverse bias light current for 30pA, 100pA, and 500pA of primary photocurrent, all of which are in the uA range at 4V reverse bias.

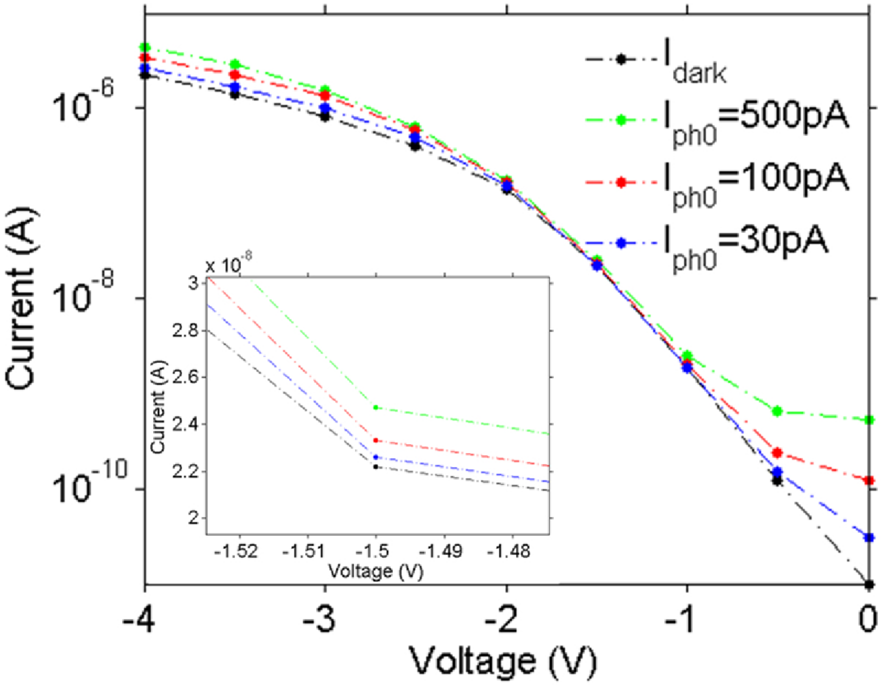

Figure 4.11: Current versus voltage for the CEP detector in dark condition and different photocurrent conditions at 1060 nm, from [21].

The gain versus bias is plotted in Fig. 4.12(a). The gain is even higher at 1060nm than that measured for 635nm, reaching 10,000. The responsivity, defined as the ratio of the output photocurrent to input optical power, is shown in Fig. 4.12(b). A responsivity of nearly 100A/W was obtained, which is orders of magnitude better than the state-of-the-art commercial 1060nm APD.

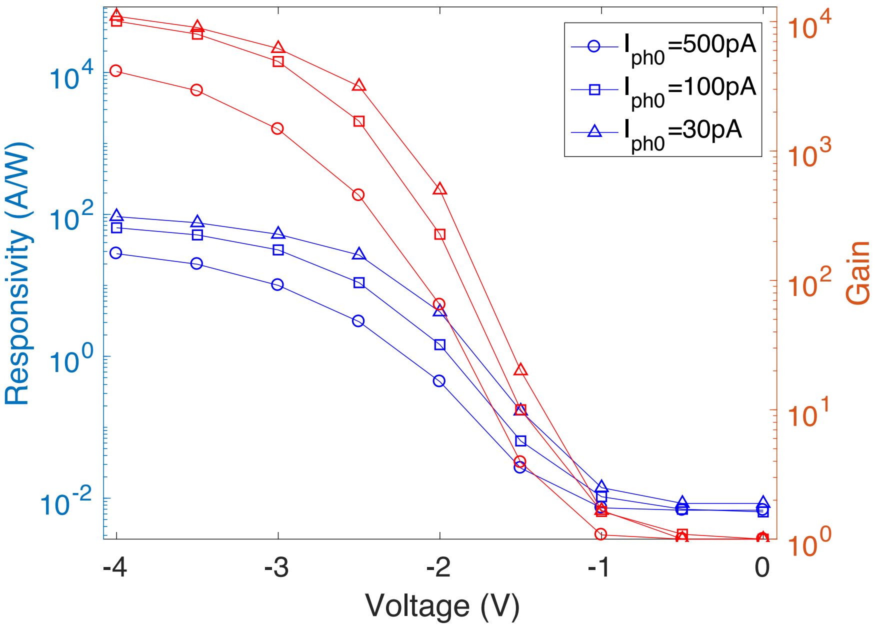

Figure 4.12: Responsivity (blue) and gain (red) vs. reverse bias voltage under 1060 nm illumination, data from [21].

We compare the responsivity as a function of device operation bias of the 1060nm CEP detector to that of detectors using laser micromachining, microdischarge devices, and porous silicon. It can be seen that the CEP detector shows comparable responsivity to the best reported results in the literature, where it should also be taken into consideration that these results are either do not use CMOS compatible processes, or make use of photoconductive gain or surface states, which is not suitable for single photon detection.

The large gain achieved in a 1060nm detector is a result of the CEP effect. In addition, the high responsivity at 1060nm in an all-silicon CEP detector can be attributed to the localization of states which relax the k-selection rule of momentum conservation, another attribute of CEP. Thus, it is notable that the localization of states inherent in the CEP process not only allows for high carrier multiplication gain at low bias but also for an enhanced responsivity to near-bandgap wavelengths. The 1060nm CEP detector not only shows superior responsivity and operation conditions compared to the top commercial 1060nm APDs, but is also offers a more scalable and CMOS compatible 1060nm all-silicon detection compared to leading research efforts.

4.6.3 Maximum Gain of 1060 nm CEP Detector

In order to verify that it is possible to obtain a gain of 10,000 in a CEP detector, we developed a physical model of CEP based on coupled rate equations to derive the steady state small signal gain. In the previous chapter, it was explained that in equilibrium, the impurities completely ionize. However, under optical excitation, by which there is an injected photocurrent into the CEP region, there will be a nonzero concentration of neutral minority impurities. Let the neutral acceptors in the n-region be defined as N_{An}^0, and the neutral donors in the p-region be defined as N_{Dp}^0, then we have:

$$N_{An}^0 = N_{An} - N_{An}^- \tag{4.7a}$$

$$N_{Dp}^0 = N_{Dp} - N_{Dp}^+ \tag{4.7b}$$

We then develop the following rate equations:

$$\frac{dN_{An}^0}{dt} = \left(\frac{I_{ph}}{qV_n} + \frac{n_p V_p}{\tau V_n}\right)(N_{An} - N_{An}^0)\Omega_X - \frac{N_{An}^0}{\tau_h} \tag{4.8}$$

$$\frac{dp_n}{dt} = \frac{N_{An}^0}{\tau_h} - \frac{p_n}{\tau} - W_h(N_{An} - N_{An}^0)p_n \tag{4.9}$$

$$\frac{dN_{Dp}^0}{dt} = \frac{p_n V_n}{\tau V_p}\left(N_{Dp} - N_{Dp}^0\right)\Omega_Y - \frac{N_{Dp}^0}{\tau_e} \tag{4.10}$$

$$\frac{dn_p}{dt} = \frac{N_{Dp}^0}{\tau_n} - \frac{n_p}{\tau} - W_e\left(N_{Dp} - N_{Dp}^0\right)n_p \tag{4.11}$$

We have used the following parameter definitions:

τ_h: time for an unoccupied acceptor in the n-region to absorb a phonon to produce a hole in the valence band [s].

τ_e : time for an occupied donor in the p-region to absorb a phonon to produce an electron in the conduction band [s].

W_h : coefficient for holes in valence band to emit phonons to transition to occupied acceptors in the n-region [cm^3/s].

W_e : coefficient for electrons in conduction band to emit phonons to transition to unoccupied donors in the p-region [cm^3/s].

Ω_X : the effective volume for Coulomb interactions between a hot electron and an ionized acceptor [cm^3]

Ω_Y : the effective volume for Coulomb interactions between a hot hole and an ionized donor [cm^3]

V_n : the effective volume in the n-region contributing to the CEP effect [cm^3]

V_p : the effective volume in the p-region contributing to the CEP effect $[cm^3]$

We simplify the analysis with the following assumptions:

$N_{An} = N_{Dp} \equiv N;\ W_h = W_e \equiv W;\ \tau_h = \tau_e \equiv T;\ \Omega_X = \Omega_Y \equiv \Omega;\ V_n = V_p \equiv V$

The total current in the device is composed of the photocurrent and the rate of generation of free carriers through phonon absorption:

$$I_o = I_{ph} + qV\left(\frac{n_e}{\tau} + \frac{p_h}{\tau}\right) \tag{4.12}$$

The large signal gain, G, and differential gain, g, are:

$$G = \frac{I_o}{I_{ph}} = 1 + \frac{qV}{I_{ph}}\left(\frac{n_e}{\tau} + \frac{p_h}{\tau}\right) \tag{4.13}$$

$$g = \frac{dI_o}{dI_{ph}} = 1 + qV\frac{d}{dI_{ph}}\left(\frac{n_e}{\tau} + \frac{p_h}{\tau}\right) \tag{4.14}$$

The rate equations can be solved through various physical approximations, algebraic manipulation and discarding higher order terms of a series expansion. The result for the small signal gain is:

$$g = G_o\left(1 - {G_o}^2 \cdot \frac{I_{ph}}{I_S}\right) \tag{4.15}$$

The maximum achievable gain for a given primary photocurrent is found by solving $\frac{dg}{dG_o} = 0$:

$$g_{max} = \frac{2}{3\sqrt{3}}\sqrt{\frac{I_S}{I_{ph}}} \tag{4.16}$$

Where $I_S = \frac{qNV}{T}$ is the effective current resulting from the free carriers generated through phonon absorption, and $G_o = \frac{1+WN\tau}{1+WN\tau-N\Omega}$ is a term that reflects the Coulomb interaction between hot carriers and ionized impurities. T can be taken to be 25ps [22] and τ is taken to be 0.1ps based on the depletion region of our device structure which is about 20nm. Based on the electron capture cross section and thermal RMS velocity of electrons, we estimate $W = 2.4\times10^{-8}\, {cm^3}/{s}$. The value of Ω corresponding to the maximum gain is given by

$$\Omega_{max} = \frac{\left(\frac{1}{N}+W\tau\right)}{\left(1+\sqrt{\frac{3I_i}{I_S}}\right)} \tag{4.17}$$

In our device structure and experiment:

$$N = 2\times10^{19} cm^{-3} \tag{4.18}$$

$$V = 35\mu m\times55\mu m\times20nm = 3.85\times10^{-11} cm^3 \tag{4.19}$$

$$I_S = \frac{(1.6\times10^{-19}C)(2\times10^{19}cm^{-3})(3.85\times10^{-11}cm^3)}{25ps} = 4.93A \tag{4.20}$$

$$\Omega_{max} = \frac{\frac{1}{2\times10^{19}cm^{-3}}+\left(2.4\times10^{-8}{cm^3}/{s}*0.1ps\right)}{1+\sqrt{\frac{3\times30pA}{4.93A}}} = 5.24\times10^{-20}cm^{-3} \tag{4.21}$$

$$G_{o,max} = \frac{1+\left(2.4\times10^{-8}{cm^3}/{s}\right)(2\times10^{19}cm^{-3})(0.1ps)}{1+\left(2.4\times10^{-8}{cm^3}/{s}\right)(2\times10^{19}cm^{-3})(0.1ps)-(2\times10^{19}cm^{-3})(5.24\times10^{-32}cm^{-3})} =$$

$$2.34\times10^5 \tag{4.22}$$

$$g_{max} = (2.34\times10^5)\left[1-(2.34\times10^5)^2\cdot\frac{30pA}{4.93A}\right] = 1.56\times10^5 \tag{4.23}$$

Thus, we finally calculate that we can achieve a gain of 10^5 in our heavily doped and partially compensated CEP detector with a primary photocurrent of 30pA. In our real device and experiment, we achieved a gain of 10^4 for a primary photocurrent of 30pA. Thus, our calculated maximum achievable gain is reasonable. The experimentally achieved gain could be lower than the calculated maximum due to current leakage from surface states at the mesa sidewalls, or due to a larger than ideal dark current arising from thermal generation and tunneling.

4.7 Conclusion

This chapter presented a CEP detector using heavily doped and partially compensated silicon to create disorder. A gain of 10^4 and responsivity of nearly 100 A/W at 1060 nm illumination was achieved in an all-silicon CEP detector. Negative feedback arising from the balance between Auger excitation and phonon absorption was found to internally control the gain mechanism, which is manifested as a host of beneficial detector properties including ultralow excess noise, higher gain with lower input optical power, gain saturation at operation bias, and higher gain at room temperature operation.

Portions of Chapter 4 have been published in the following publications: Y. H. Liu, L. Yan, A. C. Zhang, D. Hall, I. A. Niaz, Y. Zhou, L. J. Sham, and Y. H. Lo, “Cycling excitation process: An ultra efficient and quiet signal amplification mechanism in semiconductor,” Applied Physics Letters 107, 053505 (2015); D. Hall,

B. Li, Y. H. Liu, L. Yan, and Y. H. Lo, “Complementary metal-oxide-semiconductor compatible 1060 nm photodetector with ultrahigh gain under low bias,” Optics Letters 40, 19 (2015). For these papers, the dissertation author was a coauthor/ primary investigator and author.

References:

1. Y. H. Liu, L. Yan, A. C. Zhang, C. Hall, I. A. Niaz, Y. Zhou, L. J. Sham, and Y. H. Lo, "Cycling excitation process: An ultra efficient and quiet signal amplification mechanism in semiconductor," Applied Physics Letters **107**, 053505 (2015).

2. G. E. Bulman, V. M. Robbins, and G. E. Stillman, "The determination of impact ionization coefficients in (100) gallium arsenide using avalanche noise and photocurrent multiplication measurements," IEEE Transactions on Electron Devices **ED-32**, 11 (1985).

3. Y. Kang, H. D. Liu, M. Morse, M. J. Paniccia, M. Zadka, S. Litski, G. Sarid, A. Pauchard, Y. H. Kuo, H. W. Chen, W. S. Zaoui, J. E. Bowers, A. Beling, D. C. McIntosh, X. Zheng, and J. C. Campbell, "Monolithic germanium/silicon avalanche photodiodes with 340 GHz gain-bandwidth product," Nature Photonics **3**, p.p. 59-63 (2009).

4. Y. Kang, P. Mages, A. R. Clawson, P. K. L. Yu, M. Bitter, Z. Pan, A. Pauchard, S. Hummel, and Y. H. Lo, "Fused InGaAs-Si avalanche photodiodes with low-noise performances," IEEE Photonics Technology Letters, **40**, 11 (2002).

5. H. D. Liu, H. Pan, C. Hu, D. McIntosh, Z. Lu, J. Campbell, Y. Kang, and M. Morse, "Avalanche photodiode punch-through gain determination through excess noise analysis," Journal of Applied Physics **106**, 064507 (2009).

6. K. S. Lau, C. H. Tan, B. K. Ng, K. F. Li, R. C. Tozer, J. P. R. David, and G. J. Rees, "Excess noise measurement in avalanche photodiodes using a transimpedance amplifier front-end," Measurement Science Technology **17**, p.p. 1941-1946 (2006).

7. J. Y. Mun, S. Y. Jeong, J. H. Kim, S. S. Han, and I. H. Kim, "A low fluence Q-switched Nd: YAG laser modifies the 3D structure of melanocyte and ultrastructure of melanosome by subcellular-selective photothermolysis," Journal of Electron Microscopy **60**, 1 (2011).

8. G. Ku, M. Zhou, S. Song, Q. Huang, J. Hazle, and C. Li, "Copper sulfide nanoparticles as a new class of photoacoustic contrast agent for deep tissue imaging at 1064 nm," ACS Nano **6**, 8 (2012).

9. C. S. Montross, T. Wei, L. Ye, G. Clark, and Y. W. Mai, "Laser shock processing and its effects on microstructure and properties of metal alloys: a review," International Journal of Fatigue **24**, 10 (2002).

10. A. S. Afzal, A. W. Yu, J. J. Zayhowski, and T. Y. Fan, "Single-mode high-peak-power passively Q-switched diode-pumped Nd:YAG laser," Optics Letters **22**, 17 (1997).

11. R. A. Myers, R. Farrell, A. M. Karger, J. E. Carey, and E. Mazur, "Enhancing near-infrared avalanche photodiode performance by femtosecond laser microstructuring," Applied Optics **45**, 35 (2006).

12. J. E. Carey, C. H. Crouch, M. Shen, and E. Mazur, "Visible and near-infrared responsivity of femtosecond-laser microstructured silicon photodiodes," Optics Letters **30**, 14 (2005).

13. Z. Huang, J. E. Carey, M. Liu, X. Guo, E. Mazur, and J. C. Campbell, "Microstructured silicon photodetector," Applied Physics Letters **89**, 033506 (2006).

14. K. Yamamoto, A. Sakamoto, T. Nagano, and K. Fukumitsu, "NIR sensitivity enhancement by laser treatment for Si detectors," Nuclear Instruments and Methods in Physics Research Section A **624**, 2 (2010).

15. S. Hu, P. Han, S. Wang, X. Mao, X. Li, and L. Gao, "Structural and optoelectronic properties of selenium-doped silicon formed using picosecond pulsed laser mixing," Physica Status Solidi A **209**, 12 (2012).

16. S. J. Park, J. G. Eden, and J. J. Ewing, "Photodetection in the visible, ultraviolet, and near-infrared with silicon microdischarge devices," Applied Physics Letters **81**, 4529 (2002).

17. M. K. Lee, C. H. Chu, and Y. H. Wang, and S. M. Sze, "1.55-μm and infrared-band photoresponsivity of a Schottky barrier porous silicon photodetector," Optics Letters **26**, 3 (2001).

18. J. M. Shieh, W. C. Yu, C. K. Wang, B. T. Dai, H. C. Kuo, J. Y. Huang, and C. L. Pan, "Near infrared silicon quantum dots MOSFET detector," Conference on Lasers and Electro-Optics/International Quantum Electronics Conference, Optical Society of America, CFK2 (2009).

19. J. P. Zheng, K. L. Jiao, W. P. Shen, W. A. Anderson, and H. S. Kwok, "Highly sensitive photodetector using porous silicon," Applied Physics Letters **61**, 459 (1992).

20. F. Raissi and N. A. Sheeni, “Highly sensitive near IR detectors using n-type porous Si,” Sensors and Actuators A **104**, 2 (2003).

21. D. Hall, B. Li, Y. H. Liu, L. Yan, and Y. H. Lo, “Complementary metal-oxide-semiconductor compatible 1060 nm photodetector with ultrahigh gain under low bias,” Optics Letters, Vol. 40, No. 19, pp. 4440-4443, 2015.

22. T. R. Hart, R. L. Aggarwal, and B. Lax, “Temperature dependence of raman scattering in silicon,” Physical Review B Vol. 1 No. 2, 1969.

Chapter 5 Carbon-Doped Amorphous Silicon CEP Detector

5.1 Motivation for Amorphous Silicon CEP Detector

5.1.1 Properties of Hydrogenated Amorphous Silicon

In the previous chapters, it was seen that heavy doping and compensation lead to localization of states which can facilitate a reverse Auger process that occurs at much lower reverse bias and lower excess noise than that of impact ionization. In this chapter, the utilization of amorphous material to obtain localization of states is proposed. An overview of amorphous silicon is provided, which will explain why amorphous silicon is a strong candidate to realize a CEP based detector. Furthermore, it is shown how the disorder of the material can be engineered through the incorporation of a high phonon energy dopant such as carbon. Finally, device design and experimental results are given which show an amorphous silicon detector capable of exceeding THz gain bandwidth product and high sensitivity.

Amorphous silicon maintains the tetrahedral covalent bonding of silicon atoms but lacks the diamond lattice network, or any periodicity for that matter. Amorphous silicon has localized states close to the mobility band edge, as well as deep states associated with defects close to the Fermi Energy. Thus, amorphous silicon is often passivated with hydrogen during deposition in order to reduce the density of dangling bonds associated with deep states. Amorphous silicon, being amenable to thin film approaches such as chemical vapor deposition, offers ease in fabrication and is more environmentally friendly to manufacture than crystalline silicon. Thus, amorphous silicon is adopted for a variety of photovoltaic applications, despite its reduced quantum efficiency.

Amorphous silicon maintains the short-range order of crystalline silicon since both exhibit tetrahedral bonding to four neighboring silicon atoms. Amorphous silicon lacks, however, the long-range order of crystalline silicon since the latter is characterized by lattice periodicity while the former, lacks periodicity. Amorphous silicon forms a continuous random network whose order is only governed by bonding coordination, which stipulates how many bonds an atom should have within the network. The bandgap and electrical properties of amorphous silicon are not too dissimilar from crystalline silicon, with some important differences. Crystalline silicon is characterized by a periodic potential with Bloch wave solutions to the Hamiltonian. This allows a precise relation between energy and momentum, or k-vector, from which the effective masses of electrons and holes as well as the density of states can be derived. The concept of a k-vector does not apply to amorphous silicon. Thus, the momentum conservation criterion is relaxed, similar to the effect of degenerately doping a crystalline semiconductor.

Nevertheless, the density of states for amorphous silicon is still close to that of crystalline silicon. In amorphous silicon, however, there is a band tail in the amorphous silicon density of states which extends into the forbidden gap. Thus, the conduction band is no longer a sharp energy cutoff as in crystalline silicon, but rather an energy boundary between localized and extended states. Electrons in the conduction band are mobile and act as charge carriers in both amorphous and crystalline silicon. In amorphous silicon, however, there are electrons occupying states below the conduction band energy within the band tail. These states are localized. Furthermore, the amorphous silicon density of states contains deep states within the bandgap around the Fermi Energy.

Carriers in localized states, both in the band tail and in deep states, do not typically contribute to conduction unless certain mechanisms are involved. One such mechanism is hopping from one band tail state to another band tail state. This tunneling, however, is typically not a major effect except at high temperature. Tunneling between deep states is also possible, but can be ignored for hydrogenated amorphous silicon since hydrogen passivates defects that give rise to deep states.

Another effect of disorder is increased carrier scattering in amorphous silicon which reduces the free carrier mobility. While in crystalline silicon the typical electron and hole mobilities are roughly 1400 cm^2/Vs and 470 cm^2/Vs respectively [1], these values are reduced to around 15 cm^2/Vs and 2 cm^2/Vs [2] in hydrogenated amorphous silicon and are even far lower in un-hydrogenated amorphous silicon.

Because CEP requires localized states close to the mobile bands, amorphous materials are a viable candidate to realize a CEP-based detector. It is the goal of this chapter to show that the limitation of employing amorphous silicon in high sensitive optoelectronic devices, namely the low carrier mobility, can be overcome through device design exploiting the CEP mechanism. Furthermore, the localized states close to the mobility edge can be used to facilitate CEP.

5.1.2 Gain in a-Si:H

Gain in crystalline semiconductor by impact ionization, as well as gain by a similar but fundamentally different mechanism involving localized states and electron-phonon interactions, were both explained previously. We now explain the presence of both gain mechanisms in amorphous semiconductors, starting with gain by impact ionization. Impact ionization in amorphous semiconductors requires a higher breakdown field than in their crystalline counterparts due to reduction in free carrier mobility and smaller mean free path for inelastic scattering. In amorphous silicon in particular, the mean free path for inelastic scattering is estimated to be 10A, which would require 1E7 V/cm impact ionization breakdown field [2]. Nonetheless, there have been various reports of multiplication gain in amorphous silicon due to impact ionization. In 1995, an APD using an amorphous SiGe layer for absorption and amorphous silicon layer for carrier multiplication reported a multiplication gain of 686 at a bias of 16V [3].

The Lucky Drift model of impact ionization was introduced to suggest that there is a certain kinetic energy a hot carrier accelerated by an electric field needs to obtain before it can initiate impact ionization. If the carrier can reach this threshold without losing its energy through an inelastic collision, it can impact ionize (which is itself an inelastic process). However, a hot carrier can be involved in an elastic collision while still accumulating kinetic energy. Indeed, it was later realized that momentum relaxation occurs at a much faster rate than energy relaxation [4]. One question which has some uncertainty is why amorphous selenium, despite its larger bandgap and smaller carrier mobility, has a smaller required field for impact ionization than amorphous silicon. One hypothesis based on the lucky drift model is that hydrogenated amorphous silicon has a significant optical phonon energy of 80meV, compared to amorphous selenium where the energy loss due to inelastic phonon scattering was determined to be 30meV [5]. This may suggest that even though the mean free path for inelastic scattering is smaller in amorphous selenium than in amorphous silicon, the energy lost each scattering event is far less in amorphous selenium which allows it to have a significantly smaller breakdown field than in amorphous silicon.

The low mean-free path of amorphous silicon compared to crystalline silicon which decreases the mean free path of inelastic scattering, and the high phonon energy compared to amorphous selenium which increases the energy lost per scattering event, poses a significant challenge in implementing impact ionization in amorphous silicon based optoelectronic devices. However, we hypothesize that although amorphous silicon is not an ideal candidate for realizing multiplication gain through impact ionization, it is a promising candidate for realizing multiplication gain through CEP. The first reason is that CEP occurs at much lower electric field than impact ionization due to a higher probability of Auger excitation that results from localization. This means that with a sufficiently thin a-Si layer, below 100nm, we expect that a sufficient electric field across the a-Si layer can be obtained for CEP to occur despite being below the critical field for impact ionization by at least an order of magnitude. The second reason is that although stronger interactions between phonons and free carriers (compared to those in a-Se) increase the average energy lost per inelastic scattering event, it is the coupling between phonons and localized carriers in the bandtail states which will be important for an efficient gain though the CEP mechanism. Additionally, we will show that by the addition of dopants such as carbon which have high phonon energy, we can control the degree of phonon coupling to localized bandtail states.

5.1.3 Tailoring Disorder in a-Si:H through Carbon

Incorporation of certain impurities in a-Si:H can increase its disorder. Disorder is often described in terms of coordination bonding, as explained previously. Thus, introduction of impurities does not necessarily increase disorder if those impurities obey the 8-N rule. However, there are other criteria used to predict whether certain impurities will introduce disorder. For example, the Si-Si and Ge-Ge covalent bond lengths are relatively similar, 2.35 and 2.45, respectively, whereas the C-Si covalent bond length is 1.87, indicating that a Ge impurity in a-Si will be a smaller perturbation of a-Si compared to a C impurity [6]. Furthermore, carbon could potentially form certain pi-bond configurations not possible in a-Si, further increasing the perturbation from ideal a-Si and increasing the disorder.

While it has been established that carbon can increase the disorder in a-Si, it is has also been shown that the carbon content in a-Si can tailor the disorder. For example, in the Raman spectrum of crystalline silicon, there is a first order optical phonon peak at 510 cm^{-1}, also present in amorphous silicon since short range order is preserved. Additionally, in amorphous silicon, there is a broad transverse optical (TO) phonon peak at 480 cm^{-1} resulting from the relaxation of the k-selection rule. The width of the broad peak can be related to the short range order [7]. It has also been shown that incorporation of carbon increases the local structural disorder due to strain resulting from difference in covalent bond length discussed previously, and that this disorder can be determined from the TO phonon peak in the Raman spectrum [8]. A Raman spectrum of PECVD-grown a-Si:H films grown on an n-Si substrate is shown in Fig. 5.1 for no carbon content and 10% carbon content. Carbon incorporation is obtained by varying the methane concentration during deposition.

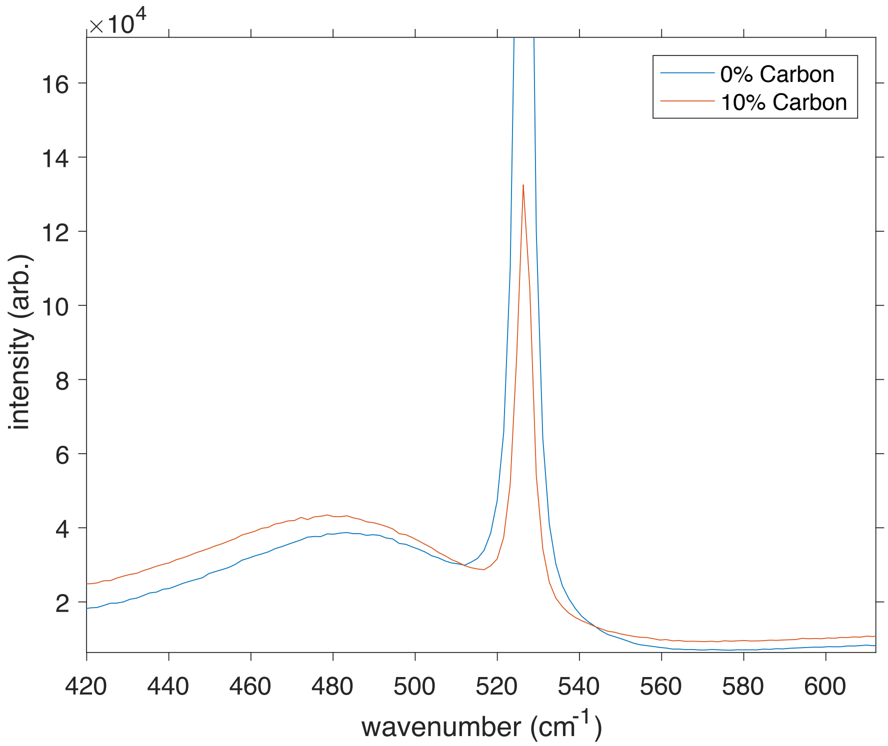

Figure 5.1: Raman spectrum of PECVD-grown amorphous silicon films grown on n-Si substrate for 0% and 10% carbon concentrations.

5.2 a-Si:H CEP Detector Principles

The cycling process is similar to that in crystalline material. The main difference is that in crystalline silicon, ionized compensating impurities provide the required localized states, whereas in amorphous silicon, the exponential band tails penetrating beyond the band edge and into the forbidden gap region provide the required localized states.

In crystalline silicon, CEP was realized through heavy doping and dopant compensation, which relaxes the k-selection rule and enhanced the probability of

Auger excitation via localized states associated with ionized compensating impurities. In amorphous silicon, the k-selection rule is intrinsically relaxed, and the Auger excitation via localized band-tail states can occur due to a thin amorphous silicon layer which can yield a substantial electric field across that layer. Although below the electric field strength required for impact ionization breakdown, the presence of strong electron phonon coupling due to carbon incorporation can lead to a CEP gain.

To describe the CEP effect in a-Si:H, we consider a thin amorphous silicon gain region on an n+-type crystalline silicon substrate with a top Indium Tin Oxide (ITO) layer for both electrical contact and light transparency. The band diagram under zero bias for this layer structure is shown in Fig. 5.2a, and also under reverse bias in Fig. 5.2b. The work function of Ar sputtered ITO, 4.3eV [9], and the electron affinities of a-Si:H and n+-type crystalline silicon are 3.8eV [10] and 4.05eV [1], respectively. The bandgaps of a-Si:H and n+-type crystalline silicon are 1.72eV [10] and 1.12eV [1]. ITO being a metal, has completely filled states beneath its Fermi level. The energy offset between the ITO Fermi level and the a-Si:H conduction band is the Schottky barrier height between ITO and a-Si:H. The Schottky Barrier height, $\mathit{\Phi}_B$, between a metal and semiconductor is given by the difference between the metal work function, $\mathit{\Phi}_m$, and semiconductor electron affinity, X :

$$\mathit{\Phi}_B = \mathit{\Phi}_m - X \tag{5.1}$$

The conduction band offset and valence band offset between a-Si:H and n+-type crystalline silicon can be found using Anderson’s rule for constructing band diagrams involving heterojunctions of different semiconducting material. Anderson’s rule states the conduction band offset is given by the difference in electron affinities between the two semiconductors, in which case the valence band offset is uniquely determined by the conduction band offset and the bandgaps of the two semiconductors. If the bandgap and electron affinity of the semiconductor whose conduction band is closer to the vacuum level are E_{g1} and X_1, respectively, and the bandgap and electron affinity of the other semiconductor are E_{g2} and X_2, respectively, then the conduction band offset and valence band offset are given by:

$$\Delta E_C = X_1 - X_2 \tag{5.2}$$

$$\Delta E_V = E_{g1} - \Delta E_C - E_{g2} \tag{5.3}$$

The result is that $\Phi_B = 0.5eV$, $\Delta E_C = 0.25\text{eV}$, and $\Delta E_V = 0.35eV$

At zero bias, ITO, a-Si:H and n+-crystalline silicon share the same Fermi level. Under reverse bias, that is, a negative bias applied to the ITO with respect to the n+-crystalline silicon substrate, the quasi-Fermi level of the n+-crystalline silicon substrate gets pushed down with respect to the ITO highest occupied level. No matter the bias, the Schottky barrier height and band offsets calculated above remain the same, and the band bending will be such that the above calculated values are satisfied. The resulting band diagram is shown in Fig. 5.2 for a relatively thin amorphous silicon layer thickness of 30 nm. Note the band diagrams represent the ideal case with no interfacial defect states. In the presence of interfacial states, a positive sheet charge could develop which would cause interfacial band bending in the amorphous silicon that would impede electron flow. This effect could reduce the quantum efficiency.

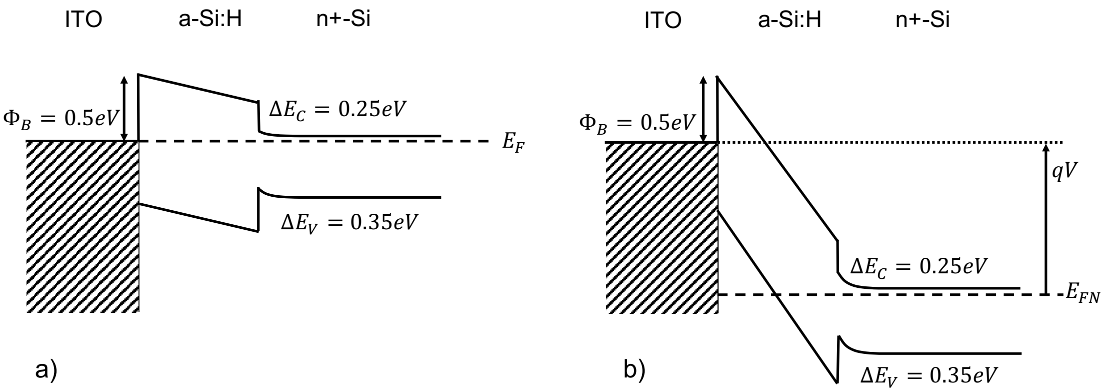

Figure 5.2: Band diagram of the ITO/a-Si:H/n+-Si CEP detector under zero bias (a) and reverse bias (b).

The full cycling process of CEP in a-Si:H is now described for this layer structure and shown in Fig. 5.3. A photon absorbed in the crystalline substrate generates an electron-hole pair. The electron, being a majority carrier, is collected at the bottom electrode. The hole is accelerated across the amorphous silicon region where it can excite an electron from the valence band to the conduction band tail, slightly below the mobility band of extended states. By doing so, a free hole is generated in the valence band which can be collected by the top electrode. The excited electron can reach an extended state through phonon interaction. This electron can then be accelerated across the amorphous silicon gain region and excite an electron from the valence band tail into the conduction band. By doing so, this creates an additional mobile electron and a localized hole. The localized hole created in the valence band tail can reach an extended state through phonon interaction, thereby completing the cycling process.

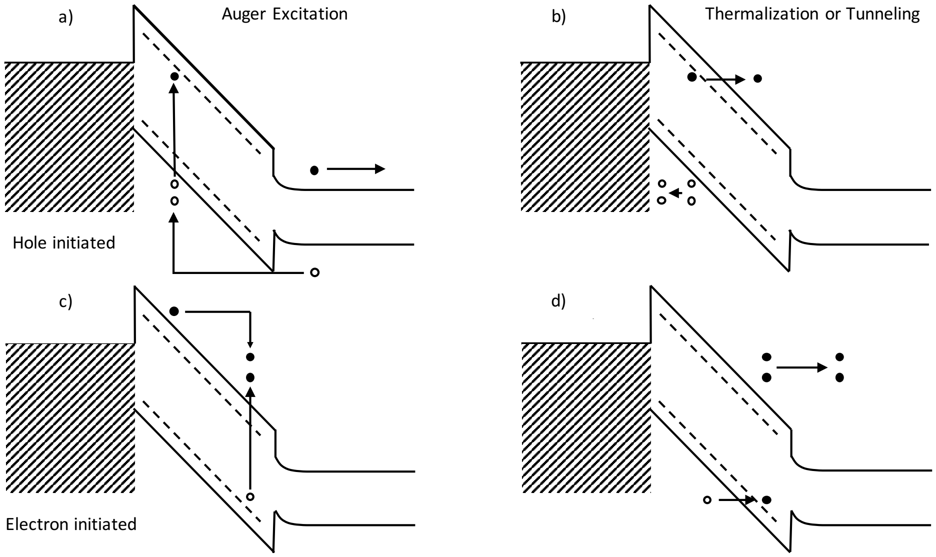

Figure 5.3: Complete cycling process in an a-Si:H CEP detector.

5.3 a-Si:H CEP Detector Design

The fabrication process of the C-doped a-Si:H CEP detector is described. The process flow and final device cross section is also shown in Fig. 5.4, numbered according to photolithography steps. A heavily-doped n-type silicon substrate is used. Amorphous silicon is grown by PECVD in an Oxford Plasmalab 80+ PECVD system using silane (SiH4) as a precursor gas for amorphous silicon deposition and methane (CH4) as a precursor gas for carbon incorporation. The growth conditions include 1500mT pressure during deposition and 270C for the sample stage. The SiH_4 flow rate is 450sccm for all depositions, with a deposition rate of roughly 0.8 nm per second.

The chamber was first conditioned for 12 minutes using this SiH_4 flow rate with no methane. Amorphous silicon samples 30 nm in thickness with 0%, 5% and 10% carbon were deposited by using CH_4 flow rates of 0sccm, 24sccm, and 50sccm, respectively. Following the amorphous silicon deposition, the amorphous silicon film was further passivated with hydrogen gas using a Trion RIE etcher. Although the amorphous silicon could become partially hydrogenated during the PECVD step, the film was further hydrogen loaded in order to passivate dangling bonds associated with deep states. H_2 could diffuse into the relatively thin amorphous silicon layer. The H_2 passivation was performed at 40C, 300mT, 77sccm H_2 gas, 50W RIE power, for 60s. Roughly 200 nm of silicon dioxide was deposited on top of the amorphous silicon. A chromium/gold metal stack of 150 nm total thickness was deposited on top of the SiO_2 by the lift-off method. The Cr/Au was used as an etch mask to etch the SiO2 layer using a buffered oxide etch down to the amorphous silicon layer. Indium Tin Oxide (ITO) was then deposited by lift-off to a thickness of 200 nm. The ITO serves both as the active area definition and also part of the top electrical contact. Since ITO is transparent, it can completely cover the light-sensitive region. A mesa etch was then performed using both ITO and Cr/Au as an etch mask to completely etch the a-Si and partially into the substrate. Finally, titanium/gold metal stacks were deposited on the top and bottom of the mesa for electrical contact.

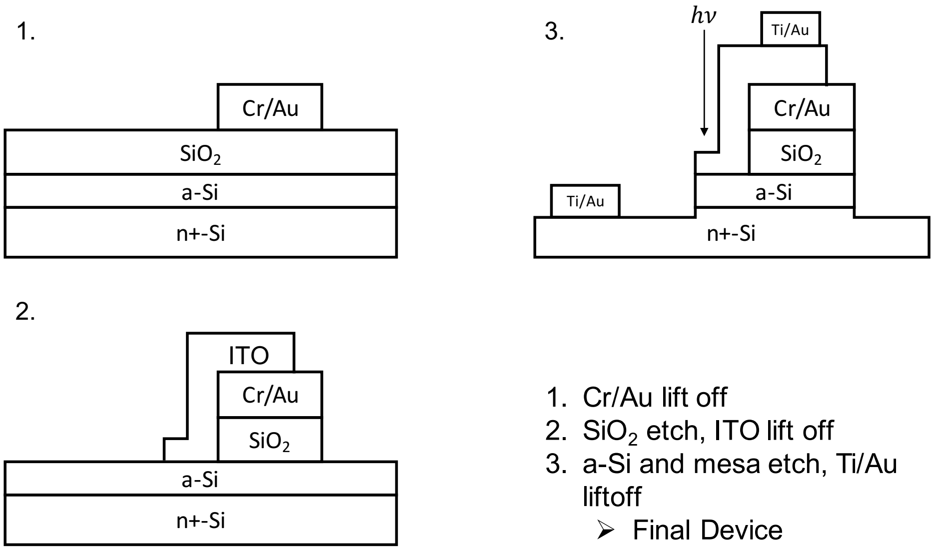

Figure 5.4: Fabrication process for the C-doped a-Si:H CEP detector.

The sample layout micrograph is shown in Fig. 5.5(a) and the detailed device top view micrograph is shown in Fig. 5.5(b). The device active area diameter was designed to vary from 15um to 30um for different rows of devices on the same die. The active area is the smaller circle as seen from the top view. The larger circle as seen from the top view is the signal contact pad, which is the top contact. The metal pattern surrounding the device is the ground contact, which contacts the bottom of the mesa. The pitch is designed to be compatible with a ground-signal-ground probe, with the signal probe contacting the top contact and the outer two ground probes contacting the contacts on the bottom of the mesa.

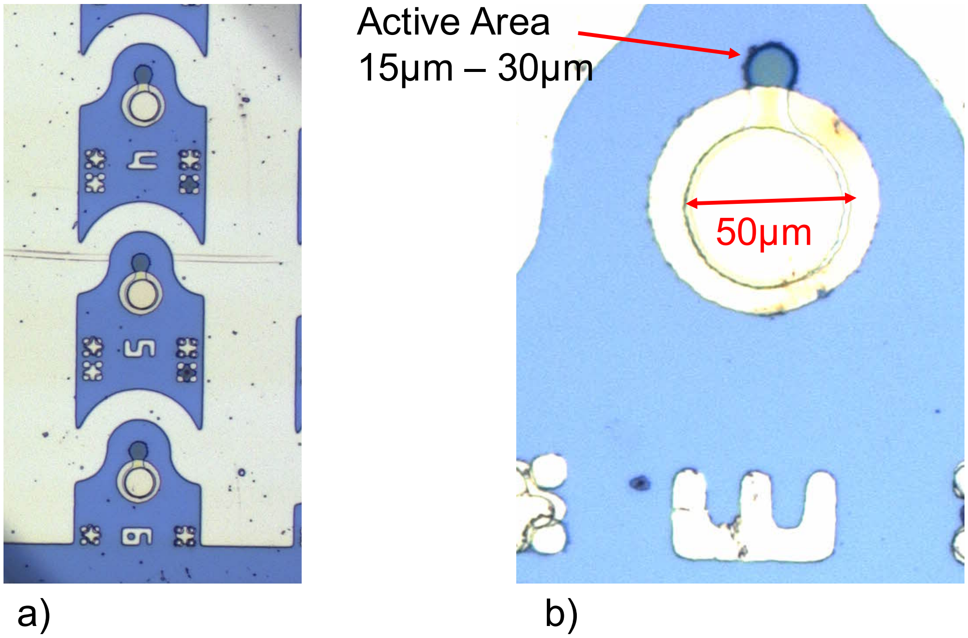

Figure 5.5: Top-view micrographs of the sample layout (a) and a single device (b).

5.4 a-Si:H CEP High Speed Characterization

Despite the low carrier mobility of hydrogenated amorphous silicon, we demonstrate that appreciable bandwidth can still be obtained using the above design with a thin, 30nm carbon doped hydrogenated amorphous silicon multiplication gain layer [11].

The optical and electrical setup for determining bandwidth is similar to that used for the high sensitivity characterization to be discussed shortly. The main differences are in the optical modulation, and the instrument used to process the output AC signal. For relatively low frequencies between 100kHz and 300MHz, amplitude modulation was applied to a 405nm laser diode with a frequency bandwidth of

300MHz. Full amplitude modulation was used to ensure that the driving current corresponding to the off state was sufficiently close to the laser threshold to ensure minimal lasing action in the off state. For each modulation frequency, the output power of the device can be determined from the power density at that center frequency as measured from an Agilent N9020A spectrum analyzer. For frequencies between 100MHz to 10GHz, a 375nm PiLas Advanced Laser Diode Systems pulsed laser diode with 40ps pulsewidth was used to illuminate the laser. This is the same laser diode used for the sensitivity characterization in the following section. The upper cutoff frequency was determined by measuring the power spectrum of the device response to the pulsed laser using the same spectrum analyzer. The different frequency components of the device frequency response is contained within the electrical pulse. The frequency range of interest is well above the laser diode repetition rate of 1MHz. The two frequency ranges, 100kHz to 300MHz and 100MHz to 10GHz, overlap in the region 100MHz to 300MHz. This region is used to calibrate the two methods of frequency response characterization and obtain consistent gain vs. frequency data over the region 100kHz to 10GHz.

A 5% carbon-doped a-Si device was used for high speed characterization. Fig. 5.6(a) shows the low dark current of amorphous silicon devices, which is even further suppressed by the incorporation of carbon. Fig. 5.6(b) shows the photocurrent gain vs. frequency for nearly three orders of magnitude for various reverse bias voltages. The gain shows high gain uniformity up to 1GHz and the gain rolloff is independent of bias voltage. The rolloff likely reflects an RC limit rather than the intrinsic performance limit of the CEP effect. Taking 1.5GHz as the intrinsic bandwidth due to CEP and a gain of 1500 at -4V reverse bias, the gain-bandwidth product is 2.25THz. This represents a higher gain-bandwidth product accomplished with thinner multiplication layer as compared to leading silicon-based APDs.

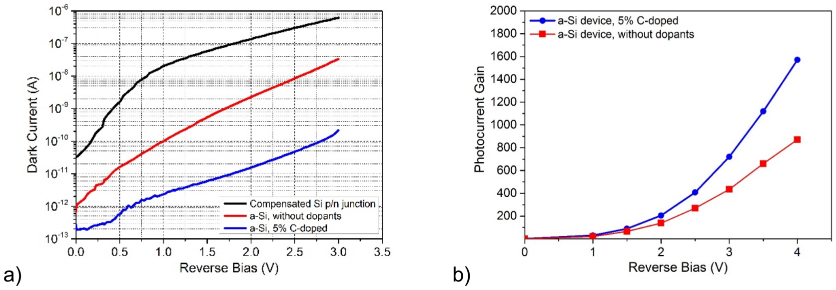

Figure 5.6: Dark current (a) and gain (b) versus reverse bias voltage for a 30 μm diameter active area C-doped a-Si:H detector with 5% carbon, courtesy of L. Yan and Y. Yu [11].

5.5 a-Si:H CEP High Sensitivity Characterization

5.5.1 Measurement with Low-Noise Amplifier

A setup for high sensitivity is shown. A pulsed 375nm PiLas Advanced Laser Diode Systems laser diode was used to illuminate the device. The wavelength used was both 635nm and 375nm. The pulsewidth is roughly 50ps and the repetition rate is 1MHz. As the output of the laser is free space, an aperture and 50X Mitutoyo infinity corrected lens are used to confine the beam onto the device active area, which is 30um in diameter. An image of the device illuminated by the 635nm laser diode is shown in Fig. 5.7.

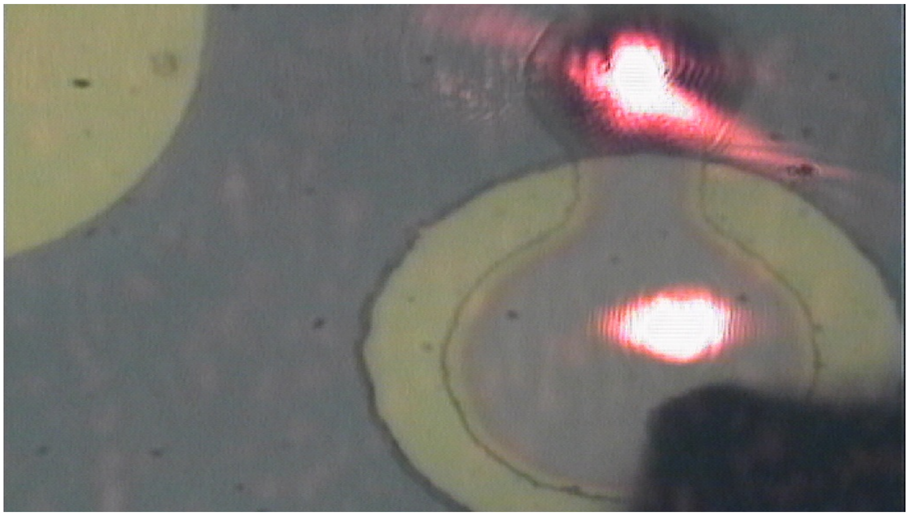

Figure 5.7: 635nm beam spot roughly 10 μm in diameter impinging on the device active area.

The measurement setup for this sensitivity measurement is shown in Fig. 5.8. The PiLAS Advanced Laser Diode is used as a pulsed optical source. A 50x Mitutoyo objective is used to focus the beam onto the active area. The device is probed using a GGB Industries Picoprobe high-speed Ground-Signal-Ground (GSG) probe with 175um pitch with 1 GHz bandwidth. The probe is SMA coupled to a Picosecond Pulse Labs 5530A bias-T. The inductive port of the bias-T is connected to a Keithley 2400 source meter for device bias. The capacitive port of the bias-T is passed to an LNA chain with total gain of 155. The AC signal is finally passed to an oscilloscope where the output electrical pulse can be seen. A representative pulse is shown.

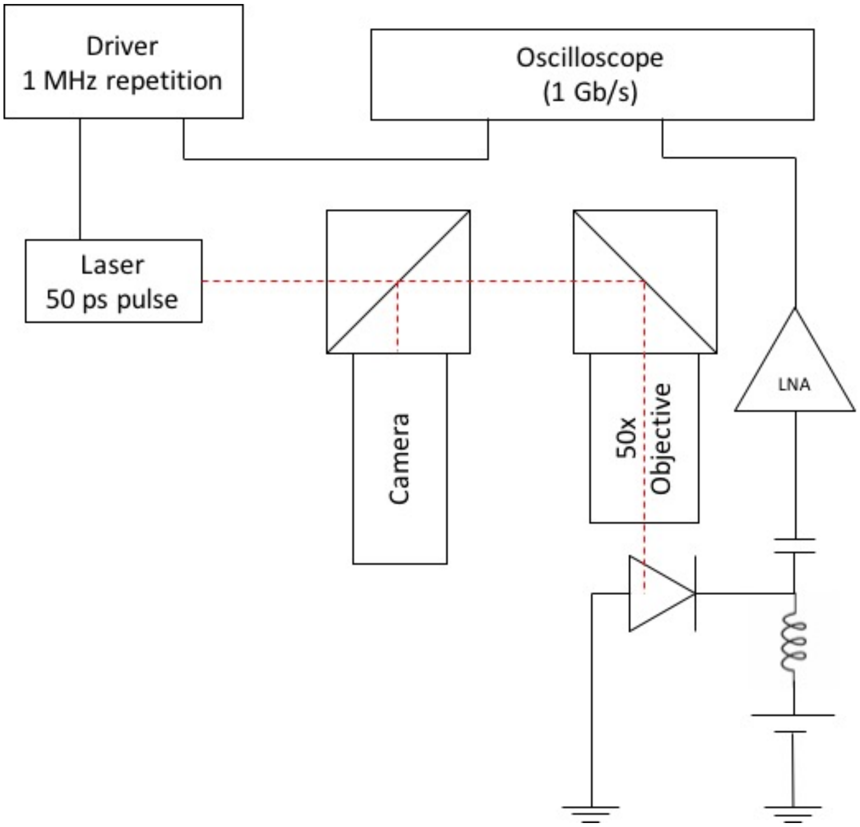

Figure 5.8: Experimental setup for sensitivity characterization of the a-Si CEP detector.

The DC gain vs. bias for different primary photocurrents is shown for a 30 μm diameter active area device in Fig. 5.9. The maximum gain reaches 10^5, which is even higher than previously reported for the heavily doped and compensated CEP detectors. Also important is that the gain increases with decreasing optical power.

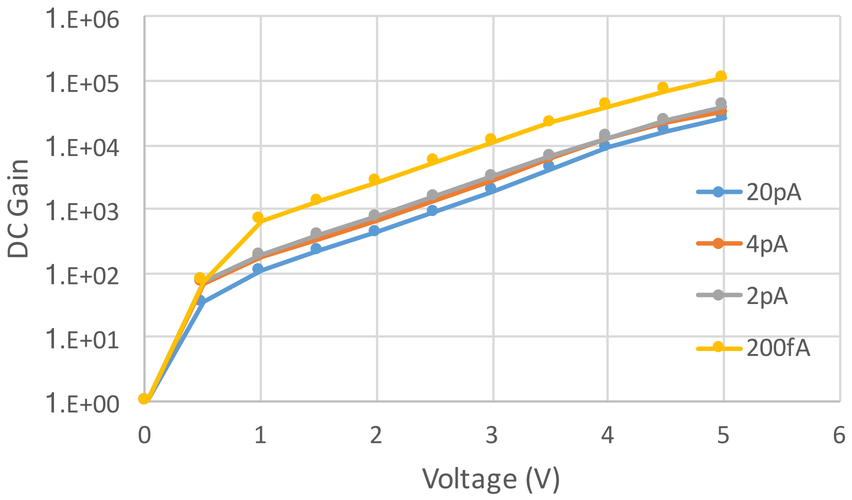

Figure 5.9: DC Gain vs. reverse bias voltage for the a-Si CEP detector under 635 nm illumination.

An example of an impulse response on the oscilloscope in response to the optical input is shown in Fig. 5.10 for a relatively high optical power. The background noise is the limiting factor in achieving single photon sensitivity. One way to overcome the background noise of the system is to use averaging. While this method is not suitable for high speed applications, it could possibly be applied to imaging applications, and also provides important information about the sensitivity capability of the detector given further improvement in system noise.

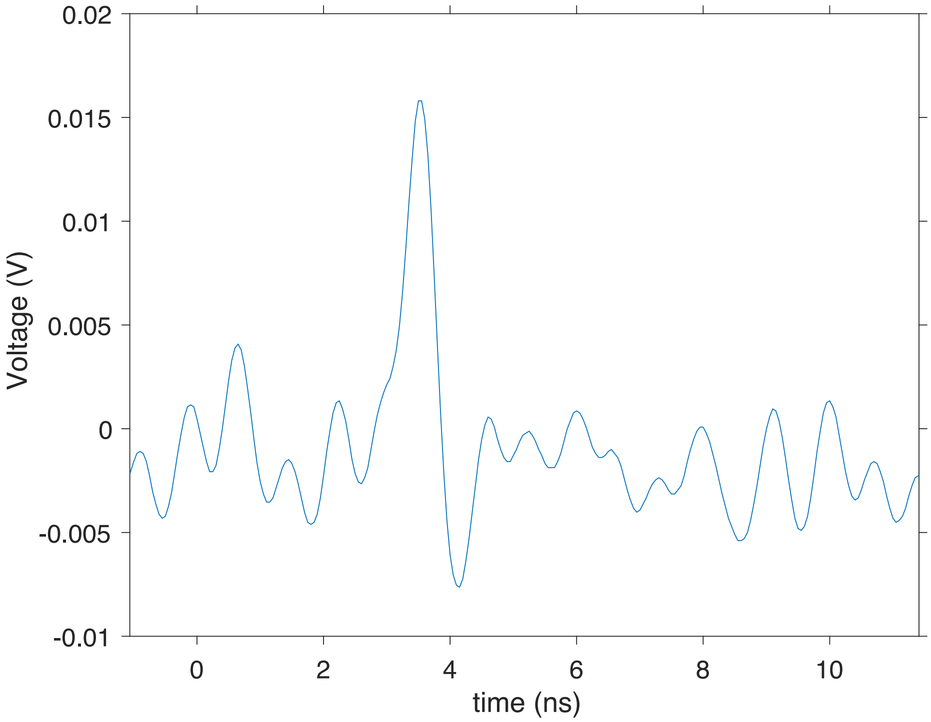

Figure 5.10: Example single-shot impulse response from the oscilloscope in response to a 635 nm input optical pulse.

The averaged oscilloscope impulse response is shown in Fig. 5.11(a). Sensitivity down to 200fA primary photocurrent is shown, which corresponds to 1.25 photons per pulse. The signal intensity as a function of photon number is shown in Fig. 5.11(b) and shows nearly two decades of dynamic range.

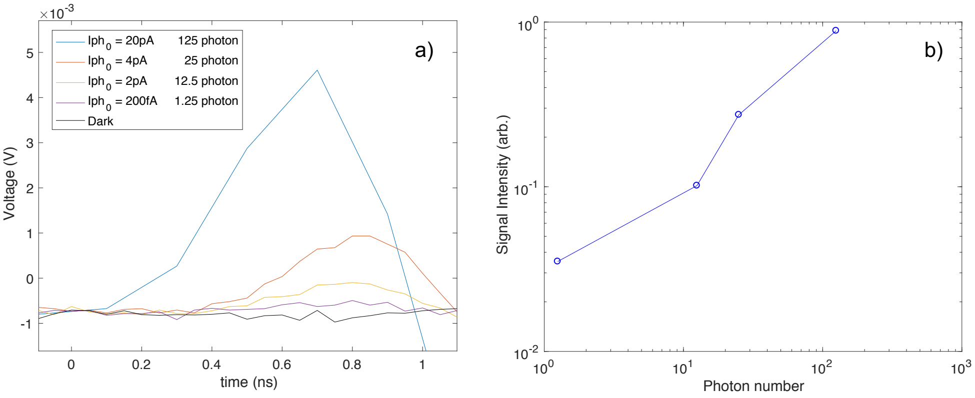

Figure 5.11: 635 nm averaged impulse response for different photon numbers (a) and signal intensity versus photon number (b).

The averaged impulse response was also performed for 375nm illumination for a 20 μm diameter active area device. We show the averaged response in the time domain in Fig. 5.12(a), with an inset showing the same response in a finer scale, with the dark subtracted. The sensitivity under 375 nm illumination is also close to the single photon level. The peak magnitude of the impulse response at 5V reverse bias is shown in Fig. 5.10(b), which similar to 635 nm illumination, shows roughly two orders magnitude of dynamic range. The impulse response indicate that the same sensitivity can be achieved with 375nm and 635nm, showing strong response in both UV and visible.

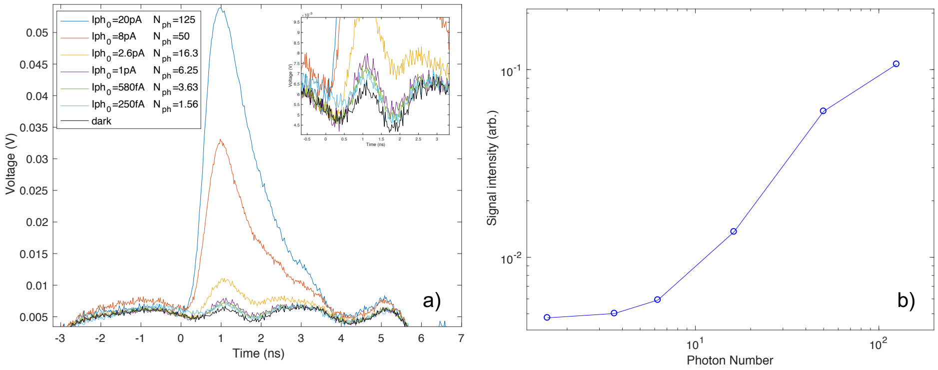

Figure 5.12: Averaged impulse response of the a-Si CEP detector in response to 375 nm pulsed illumination (a), and signal intensity versus photon number (b).

The gain at 5V under 375 nm pulsed illumination is shown in Fig. 5.13, measured at both DC and from the time averaged electrical pulse. The gain from the averaged impulse response is found by integrating the area under the curve to find the total charge based on the following equation

$$M(I_{ph0}) = \frac{1}{M_{LNA}\cdot R\cdot T\cdot I_{ph0}}\int_{t_0}^{t_1} V(t)\,dt \tag{5.4}$$

where $M_{LNA}$is the gain of the LNA and attenuator chain, which is around 155, R is the impedance, 50-ohm, $T$is the period, 1 μs, t_0 and $t_1$define the pulsewidth over which to integrate, typically between 1ns and 2ns, and $V(t)$ is the signal voltage at a given time. The integration is a numerical trapezoidal integration of the data, which can be done for each photon number. The DC gain and integrated gain are close to each other, and both show increasing gain with decreasing optical power, which is one signature of the CEP effect and very important for low light level detection.

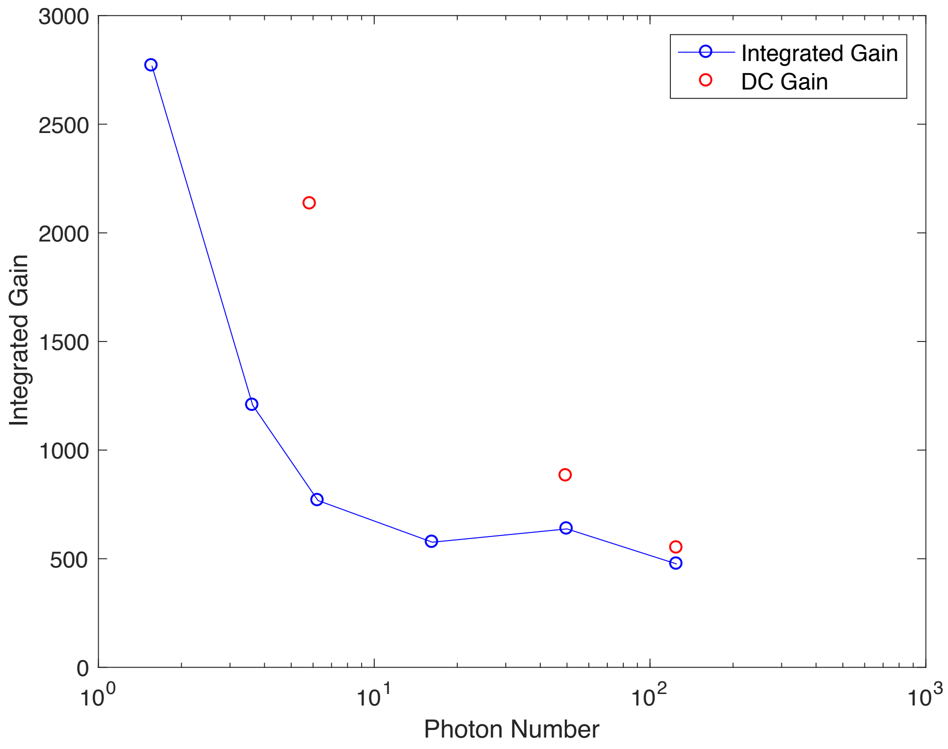

Figure 5.13: Integrated gain and DC gain versus photon number for the a-Si CEP detector under 375 nm illumination.

5.5.2 Motivation for Low Noise Circuit Design

While the averaged results are promising, it is desirable for many situations including high speed characterization to demonstrate single photon sensitivity by a single shot, without any averaging. This requires careful amplifier selection and setup design.

Any photodetector requires one or more amplifier stages to generate a detectable signal from the photocurrent. A single photon detection setup in particular requires careful amplifier selection to assure that the detector current is above the amplifier noise current. A Low Noise Amplifier (LNA) typically offers high bandwidth exceeding 1 GHz. The tradeoff of high bandwidth is higher input noise current, which arises from the thermal noise. The spectral density of the thermal noise current resulting from the amplifier is given by

$$i_n = \sqrt{\frac{4k_BT}{R}} = \sqrt{\frac{4 \cdot 1.38 \times 10^{-23} JK^{-1} \cdot 298K}{50\Omega}} = 18\, pA/\sqrt{Hz} \tag{5.5}$$

For a typical LNA bandwidth of 1GHz, this corresponds to 574nA. The LNA noise current is too high to suffice for linear mode single photon detection, as will be shown soon. The LNA is suited for Geiger mode single photon detection where the noise is not a relevant parameter. For high sensitive sub-geiger mode operation, however, a different amplifier type is typically chosen due to the critical balance between noise and sensitivity.

A transimpedance amplifier (TIA), although typically offering a smaller bandwidth than an LNA, can offer lower input noise current. Thus, a TIA is widely used as a preamplifier for APDs in optical fiber communications receivers as a preamplifier. The role of the preamplifier is to convert the photocurrent from the photodiode into a voltage, which can then be passed to a later amplifier stage such as an LNA. The photocurrent is amplified with a certain transimpedance gain, given by the ratio of output voltage to input current.

The amplifier noise requirements for a single photon detection system depends on the desired bandwidth and photodetector internal gain and noise. For pulsed laser illumination using optical attenuation to control the input photon number per pulse, it was already determined that the number of photons per pulse is given by $N_{ph} = \frac{I_{pho}T}{q}$ for a given primary photocurrent and laser repetition period. This means that the average primary DC photocurrent at 0V bias must be around 200fA for the 1us repetition period used in our setup. A PiLAS advanced laser diode is used with pulsewidth of 50ps. The single photon peak is much broader due to quenching time of the device and is around 1ns, limited by the sampling rate of the oscilloscope. The device gain is given as $M = \frac{I_{peak} \times PW}{qN_{ph}}$ where PW is the electrical pulsewidth of the device. Assuming a device gain of 500 with unity excess noise factor, the TIA must be able to detect 80nA peak current for single photon detection. Assuming we would like to detect the electrical pulse response to within 1ns, the TIA would need 500MHz of bandwidth. Thus, for the 80ns peak pulse to be above the noise of the TIA, the spectral density of the noise current must be within 4pA/√Hz. Thus, from the previous calculation of 18pA/√Hz for the LNA, the LNA would not suffice for single photon detection.

5.5.3 Circuit Design for Low Noise a-Si CEP Detector

Based on these criteria, we select a MAXIM Integraged 3658 TIA with 580MHz bandwidth and 18k-ohm transimpedance gain. The input referred noise is 45nA measured at 467MHz. This gives a noise spectral density ipsd of 2pA/√Hz which is within the requirements of single photon detection assuming a device gain of 500.

Another way of assessing the TIA performance is to consider that the number of electrons produced by the TIA within a measurement interval must be greater than the noise spectral density normalized by the TIA bandwidth: $\frac{eM}{\Delta t} > i_{psd}\sqrt{BW_{device}}$ where $\Delta t = \frac{1}{BW_{device}}$ and BW is the bandwidth corresponding to the measurement of the input referred noise. Thus, the required gain for single photon detection for the MAXIM Integrated TIA is

$$M > \frac{i_{psd}}{e\sqrt{BW_{device}}} = \frac{2pA/\sqrt{Hz}}{(1.6\times10^{-19}C)\sqrt{580MHz}} = 521 \tag{5.6}$$

which is similar to the device gain assumption we made previously.

The PCB layout including the TIA is shown in Fig. 5.14. A sample containing the photodetector is mounted on a pad using silver paste or epoxy. The signal and ground are wirebonded to coplanar waveguides. A bias-T is used in front of the TIA to allow a DC bias to be applied to the photodetector and the AC component of the photodetector current, containing the pulse, to be passed to the TIA. Since the MAX3658 has a differential output, an MPGA-105+ dual matched amplifier was used to amplify the output of the TIA. A TC1-1-13M+ rf-transformer was used to convert the differential amplifier output to a single-ended output. The PCB was also made to be 75-ohm in order to match the 75-ohm output impedance of the TIA.

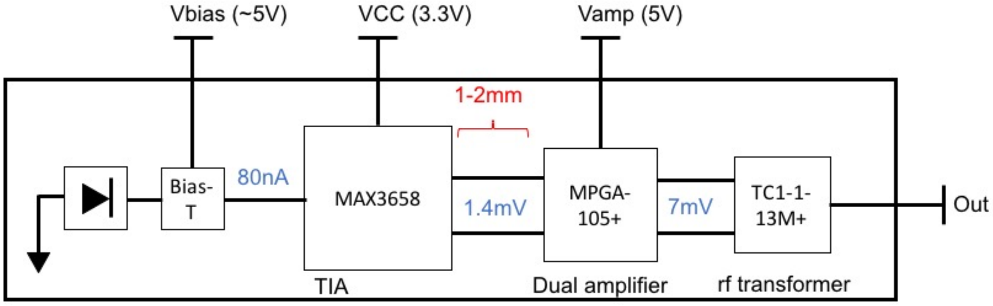

Figure 5.14: Block diagram of printed circuit board (PCB) design for the CEP a-Si detector assuming device gain of 500.

The PCB was calibrated using a sinusoid function generator rather than device at the detector input. The calibration setup is shown in Fig. 5.15. A 50-ohm resistor and 1.58k-ohm resistor were soldered on to the board only for calibration. The TIA and dual amplifier were biased according to the specifications, and the output was measured with an oscilloscope. The noise floor of the system is 10Vpp, or 5V amplitude. It was found that the input power from the function generator required to get a signal to exceed this noise level was -65dBm. This corresponds to the power from the function generator into the 50-ohm resistor soldered onto the board. The power from the function generator is given by $P_{rms} = \frac{10^{-65/10}}{1000} = 316\ pW$. Noting that the peak voltage is related to the root mean square voltage as $V_{rms} = V/\sqrt{2}$, the power is related to the input peak voltage as $P_{rms} = \frac{{V_{rms}}^2}{R} = \frac{V^2}{2R}$. The peak voltage is then $V = \sqrt{2 \cdot 50\Omega \cdot 3.16\times 10^{-10}} = 178\ \mu V$. The input peak current is $I_{peak} = \frac{178\ \mu V}{2\ k\Omega} \approx 90\ nA$.

The 2 kΩ resistance comes from the 1.58 kΩ resistor soldered onto the board and the 400Ω input resistance of the MAX3658. 90nA peak current is close to the 80nA peak assumed previously assuming a device gain of 800 with a 500MHz bandwidth. The theoretical maximum possible voltage at the output given a 90nA peak current at the input is given by $V_{max} = 90nA \cdot 18k\Omega \cdot 10^{14.4/20} = 8.5\ mV$. After accounting for a -0.5dB (10%) loss through the RF transformer and -0.3Db (7%) loss through the bias-T, the maximum voltage we could hope to see at the output would be $V_{max} = 7.1\ mV$. Thus, the 5mV we obtain at the output from a 90nA input peak current is not far from ideal.

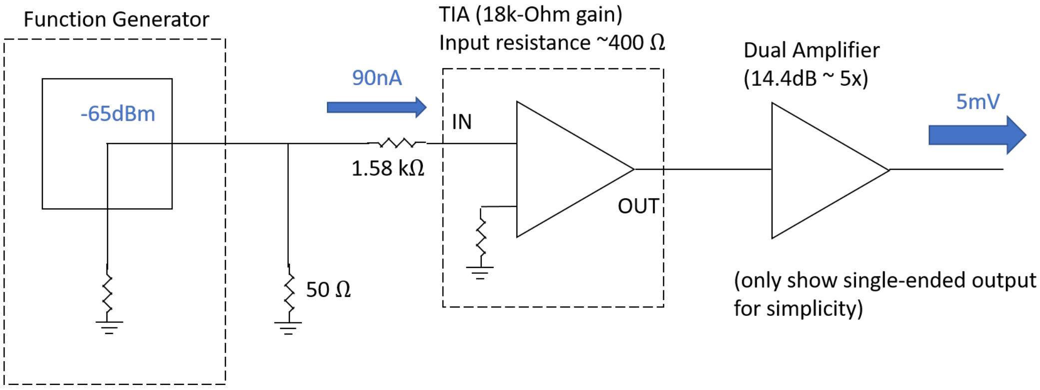

Figure 5.15: Measurement diagram for PCB calibration

5.6 Conclusion

An amorphous silicon CEP detector with carbon doping was shown to have high gain-bandwidth product and single photon sensitivity. At present, single photon sensitivity was shown for the averaged impulse response, which may be valuable for imaging but not suitable for high speed applications such as communications. Thus, a noise reduction design was introduced involving a Maxim Integrated 3658 Transimpedance Amplifier with 18 k-ohm transimpedance gain, 580 MHz bandwidth. While below the intrinsic a-Si CEP device bandwidth, 580 MHz is sufficient to resolve single photon pulses. The 45 nA_{rms} input referred noise meets the requirements for single photon detection assuming a device gain of 500, which we have shown our devices are capable of achieving considering both DC and charge integration of the pulse.

A PCB was implemented to realize this design, and successfully calibrated using a photodiode emulation method based on the desired photogenerated peak current arising from the optical pulse. Remaining challenges include device packaging, in which wedge bonding must be performed in order to make contact to the 50 μm pad. While simple in theory, the act of ultrasonic bonding can degrade the dark current and even short the device. A tradeoff between contact pad size, ideally small to reduce capacitance and maintain high bandwidth, and ease of packaging is thus a challenge. Careful optimization of pad size and ultrasonic bonding power is critical.

Portions of Chapter 5 are currently being prepared for submission for publication of the material. L. Yan, Y. Yu, A. C. Zhang, D. Hall, I. A. Niaz, M. A. R. Miah, Y. H. Liu, and Y. H. Lo, “An amorphous silicon photodiode with 2 THz gain-bandwidth product based on cycling excitation processes”; D. Hall, Y. H. Liu, L. Yan, Y. H. Lo, “Approaching the quantum limit of photodetection in solid state photodetectors,” IEEE Transactions on Electron Devices. The dissertation author was a coauthor/primary author of this material. The dissertation author would also like to

acknowledge Professor Julio Barreiro and Paul Lauria for assistance in PCB layout and purchase.

References:

1. C. C. Hu, *Modern Semiconductor Devices for Integrated Circuits*, Pearson Higher Education, New Jersey, 2010.

2. R.A. Street, Hydrogenated amorphous silicon. Cambridge University Press, 1991: New York.

3. K. H. Lee, Y. K. Fang, and G. Y. Lee, “A normal amorphous silicon-based separate absorption and multiplication avalanche photodiode (SAMAPD) with very high optical gain,” IEEE Transactions on Electron Devices, **42**, 11 (1995).

4. S. Kasap and J. A. Rowlands, S. D. Baranovskii, and Kenkichi Tanioka, “Lucky drift impact ionization in amorphous semiconductors,” Journal of Applied Physics **96**, 4 (2004).

5. A. Reznik, S. D Baranovskii and O. Rubel, G. Juska, S. O. Kasap, Y. Ohkawa and K. Tanioka, and J. A. Rowlands, “Avalanche multiplication phenomenon in amorphous semiconductors: amorphous selenium versus hydrogenated amorphous silicon,” Journal of Applied Physics **102**, 053711 (2007).

6. J. Bullot, and M. P. Schmidt, “Physics of amorphous silicon-carbon alloys,” Physica Status Solidi (b) **143**, 2 (1987).

7. J. S. Lannin, L. J. Pilione, and S. T. Kshirsagar, “Variable structural order in amorphous silicon,” Physical Review B **26**, 6 (1982).

8. A. Morimoto, S. Oozora, M. Kumeda, and T. Shimizu, “Raman studies on local structural disorder in silicon-based amorphous semiconductor films,” Solid State Communications **47**, 10 (1983).

9. K. Sugiyama, H. Ishii, and Y. O. Seki, “Dependence of indium-tin-oxide work function on surface cleaning method as studied by ultraviolet and x-ray photoemission spectroscopies” Journal of Applied Physics **87**, 295 (2000).

10. R. Stangl, A. Froitzheim, and W. Fuhs, “Thin film silicon emitters for crystalline silicon solar cells, epitaxial, amorphous or microcrystalline? – A simulation study,” Proceedings of the PV in Europe-from PV Technology to Energy Solutions (2002).

11. L. Yan, Y. Yu, A. C. Zhang, D. Hall, I. A. Niaz, M. A. R. Miah, Y. H. Liu, and Y. H. Lo, “An amorphous silicon photodiode with 2 THz gain-bandwidth product based on cycling excitation process,” under preparation.

Chapter 6 Conclusions and Outlook

This thesis presented two main approaches at overcoming limits in conventional solid state photodetectors. The ultimate goal is a detector that has the following properties:

- single photon sensitivity
- wide dynamic range > 20dB (two orders of magnitude)
- low operation bias <5V
- high speed >10 GHz

This could enable emerging applications in quantum key distribution, time resolved imaging, and on-chip silicon photonics. So far, SPADs can achieve single photon sensitivity, and APDs can achieve high speed and wide dynamic range, but no single detector utilized on a wide scale has all of these characteristics.

First, a coupled gain mechanisms device concept was introduced which uses bipolar gain. Coupling gain mechanisms in a single device has the following key attributes:

1. Reduces avalanche gain required to achieve a given overall gain
2. Restricts gain fluctuation and excess noise by virtue of the negative feedback between avalanche and bipolar gains

A model based on current continuity offers insight into how to optimize the degree of negative feedback by adjusting the electron and hole escape times, which could be done through bandgap engineering in a practical device. The MAGIC detector was experimentally realized in the InP-InGaAs material system. 10 photon sensitivity was obtained at a bit error rate of 10-2, only 6 photons from the ideal quantum limit. The BER at 35 photon sensitivity is around 10^{-8}. For comparison, InP APDs used in optical fiber communications require roughly 1000 photons to achieve a BER of 10^{-9}. A Monte Carlo model was also developed which verifies the MAGIC detector has wide dynamic range and single photon sensitivity capability with a high SPDE.

Next, an alternative signal amplification mechanism in semiconductors was introduced. Cycling Excitation Processes uses localized states in disordered material to relax the k-selection rule and increase the probability of carrier excitation into the mobile band. Furthermore, electron-phonon coupling, which is enhanced for localization of states, is key to the cycling process. Thus, CEP can be summarized to have two critical components:

1. Auger excitation: Unlike the impact ionization, which is a band-to-band Auger excitation, CEP utilizes impurity-to-band Auger excitation, a process which can occur at far reduced bias due to relaxation of momentum conservation and enhanced excitation probability.
2. Phonon absorption: electron-phonon coupling, which is enhanced for localization of states, completes the cycling process by enabling electron transitions involving shallow localized states.

CEP was first demonstrated in heavily doped and partially compensated silicon. Minority acceptors in the n-region and minority donors in the p-region are the localized states which participate in CEP. Auger excitation creates free carriers by neutralizing the impurities, and phonon absorption results in the re-ionization of those impurities. A number of merits of CEP detectors using heavy doping and compensation were realized:

- Gain of nearly 5000 at 3V reverse bias under 635 nm illumination
- Excess noise factor of 1.33 at a gain of over 2000
- Increasing gain with decreasing optical power, favoring high sensitivity
- Increasing gain with increasing temperature, favoring room temperature operation
- Gain of 10^4 and responsivity of 100A/W at 4V reverse bias under 1060 nm illumination

A physical model based on rate equations was also used to verify that the maximum achievable gain in our CEP detector under 1060 nm illumination is 10^5.

CEP was subsequently demonstrated in carbon-doped hydrogenated amorphous silicon. Amorphous silicon, by virtue of localization of shallow states, relaxes momentum conservation and increases electron-phonon coupling, vital to CEP. Hydrogen loading was used to passivate the undesired deep levels. Furthermore, introduction of carbon allows the tailoring of disorder. A CEP C-doped a-Si:H detector was developed, which demonstrated:

- Drastic dark current reduction compared to heavily doped CEP devices
- Suppression of dark current with incorporation of carbon

- Increasing gain with carbon loading
- High gain between 2000 and 10^5
- 1 GHz bandwidth and 2.25 THz gain-bandwidth product
- single photon sensitive capability using averaged impulse response

Additionally, a circuit design was presented, which is expected to significantly reduce the system noise floor and improve the signal to noise ratio. This will be vital for achieving single photon sensitivity in single shot mode rather than averaging, which is required for communications. The PCB is fully developed and calibrated, and expected to deliver promising results for the C-doped a-Si:H CEP detectors in the near future.